HOKKAIDO UNIVERSITY

Title	Study on Under-determined Problem for Wireless Communication Systems
Author(s)	上橋, 俊介
Degree Grantor	北海道大学
Degree Name	博士(工学)
Dissertation Number	甲第15214号
Issue Date	2022-09-26
DOI	https://doi.org/10.14943/doctoral.k15214
Doc URL	https://hdl.handle.net/2115/87291
Type	doctoral thesis
File Information	Shunsuke_Uehashi.pdf

Doctoral Dissertation

Study on Under-determined Problem for Wireless Communication Systems

Graduate School of Information Science and Technology
Hokkaido University

Shunsuke Uehashi

2022

Contents

Chapter 1

Introduction

1.1 Background

In wireless communications, reconstructing an unknown signal vector from linear/nonlinear measurements is a common problem. For example, in a MIMO (Multiple-Input Multiple-Output) system [1], [2], where multiple antennas are used at the transmitting and receiving sides, it is necessary to estimate the transmitted signal vector (unknown) from the received signal vector (known). Also, there are similar problems, including multi-user detection, in which user packets arriving at the base station are detected in a wireless communication system that accommodates many terminals at a single base station: equalization technology, in which signals sent out from a transmitter are received distorted in a convolutional channel and the distortion is compensated: and direction of arrival estimation technology, a type of array signal processing. In these problems, if the dimensions of the unknown vector are more than the dimensions of the observed vector, it becomes an under-determined problem that cannot be solved accurately.

For under-determined problems in such wireless communication systems, reconstruction methods using compressed sensing have been investigated. Compressed sensing is a signal processing technique to reconstruct high-dimensional sparse (most of the elements are zero) signals from a small number of measurements, and has attracted much attention in many fields [3], [4]. Quantitatively speaking, if the true solution is known in advance to be a sparse signal, compressed sensing solves the simultaneous equations $v = Cu$. Here, v denotes an M dimensional observation vector (known), C is an $M \times K$ observation matrix (known), u denotes a K dimensional original signal vector (unknown), and $K > M$ holds. In the above situation, vector u cannot be uniquely reconstructed from vector v. When u is sparse, however, it can be reconstructed using the compressed sensing technique. The compressive sensing technique is being considered for application to various wireless communication system needs, such as Direction of Arrival (DOA) estimation

and channel estimation [4]. In this paper, compressed sensing is also used to estimate the DOA and Doppler frequency of radio waves. In addition, in recent years, algorithms for compressed sensing have been used to obtain unknown vectors, not from the sparsity of the unknown vectors, but from the discrete nature of the unknown vectors [5].

In the field of overloaded MIMO [6], where the number of receiving antennas is smaller than the number of transmit streams due to receiver-side constraints, many nonlinear signal detection methods have been investigated to overcome the under-determined problem. Maximum Likelihood Detection (MLD) is the method that provides the optimal characteristics in signal detection schemes for overloaded MIMO, but its computational complexity increases exponentially in proportion to the number of transmit streams. However, there are several other signal detection methods that offer reduced computational complexity. One of these, demodulation based on BP (Belief Propagation), is known as a MIMO signal detection method that can obtain near-optimal characteristics. BP is a method to efficiently calculate the posterior probability by repeatedly passing messages on a factor graph consisting of variable nodes and observation nodes [7], [8].

On the other hand, one possible approach to solving the under-determined problem in wireless communication is to transform the under-determined problem into some form of over-determined or determined problem. If the dimensions of the observed vector M are more than the dimensions of the unknown vector $K(K \geq M)$, it may be possible to find a solution as a simple linear problem.

This paper focuses on this approach and propose methods to improve communication quality by converting the under-determined problem into some form of over-determined or determined problem in four different wireless communication systems.

1.2 Under-determined Problem Considered in this Paper

1.2.1 Novel Channel Prediction in Multi-user MIMO system

In Chapter 2[1], the author proposes a novel channel prediction scheme in multi-user MIMO system.

In multi-user MIMO systems, a base station requires downlink channel state information for each user to suppress interference. In time-varying environments, however, channels at the actual time of transmission differ from the estimated ones because there is delay. This causes interference and degrades the packet error rate performance. To solve this problem, it is proposed that a channel prediction method be based on DOA and Doppler frequency estimation of the multipath components obtained by compressed sensing techniques. Here, if the number of multipath components is larger than the number of RX antennas at the user equipment, an under-determined problem need to be solved. This problem is solved by increasing the virtual number of RX antennas and having a larger

---

[1]Chapter 2 is based on "Prediction of time-varying multi-user MIMO channels based on DOA estimation using compressed sensing" [9], by the same author, which appeared in IEEE Trans. Veh. Technol., vol. 68, no. 1, pp. 565--577, Copyright©2019 IEEE.

$M < N$

$M > N$

$$M\ \boxed{\mathbf{y}(t)}\ =\ \boxed{\mathbf{C}}\ \boxed{\mathbf{x}}\ N$$

Observed signal vector (known)

Dictionary matrix (known)

Multipath components (unknown)

$$MP\ \boxed{\begin{array}{c}\mathbf{y}(t_1)\\ \mathbf{y}(t_2)\\ \vdots\\ \mathbf{y}(t_{P-1})\end{array}}\ =\ \boxed{\mathbf{C}'}\ \boxed{\mathbf{x}}\ N$$

#N-1

Multipath components #0 ···

#0 Y Y ·· Y #M-1

UE

RX antennas (M)

#N-1

Multipath components #0 ···

#0 Y Y ·· Y #M-1 #0 Y Y ·· Y #M-1

UE (t_0) - - -> UE (t_{P-1})

Virtual RX antennas (MP)
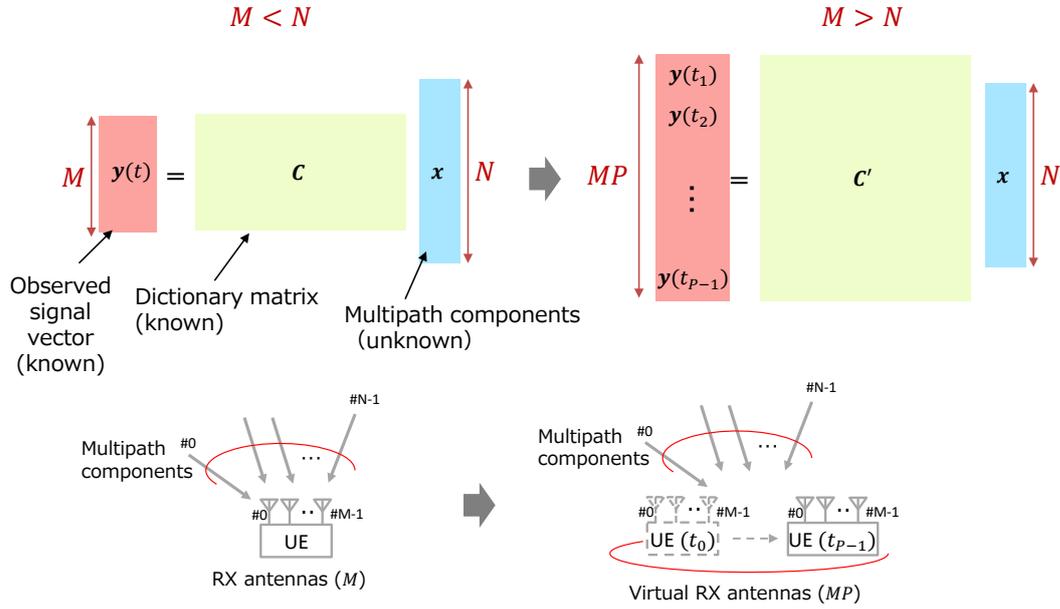
Figure 1.1: Illustration for Chapter 2.

synthetic array using the observed signals obtained at multiple times. Figure 1.1 shows an illustration of this.

1.2.2 Co-Channel Interference suppression for DSTBC transmission

In Chapter 3[2], the author proposes a novel co-channel interference supression for DSTBC transmission.

In the frequency reuse-1 scheme in which all the resources are used in every cell, CCI (Co-Channel Interference) at the cell edge may be critical. Also, compared with single antenna transmission, greater CCI is observed in DSTBC (Differential Space-Time Block Coding) using multiple antennas. For example, it is assumed that a user equipment with two antennas is located at the edge of a cell and receives DSTBC signals from two base stations. Since the number of arriving waves is greater than the number of receiving antennas, the receiver cannot demodulate distinguish all the arriving signals, which is also called an under-determined problem. To overcome this under-determined problem, the proposed method increases the dimensionality of the RX signal vector by expanding the channel matrix and the RX signal vector based on the DSTBC coding rule. This converts

---

[2]Chapter 3 is based on "Co-channel interference suppression for DSTBC transmission in single frequency network" [10], by the same author, which appeared in IEICE Trans. Commun. (Japanese Edition), vol.J105-B, no. 5, pp.446–453, Copyright©2022.

Figure 1.2: Illustration for Chapter 3.

the under-determined problem into a determined problem form and suppresses the interference even when the number of incoming interfering waves is more than twice the number of receiving antennas. Figure 1.2 shows an illustration of this image.

1.2.3 An Adaptive Equalization Scheme for wideband satellite communication

In Chapter 4[3], the author proposes a novel adaptive equalization scheme for wideband satellite communication.

In wideband satellite transmission, the communication quality deteriorates due to nonlinear and linear distortion caused by the analogue characteristics of the transmitters and receivers. In order to overcome this problem, we propose an adaptive equalizer utilizing a memory polynomial, which compensates both the nonlinear distortion caused by amplifiers and the linear distortion in the BPFs (Band Pass Filters). In this method, a linear equalization part using a conventional linear filter and a non-linear equalization part using a polynomial filter are arranged in parallel, and their outputs are combined to compensate

---

[3]Chapter 4 is based on "An adaptive equalization scheme based on memory polynomial for compensating both linear and nonlinear distortion" [11] and "An adaptive nonlinear equalizer utilizing memory polynomial for wideband satellite communications," [12], by the same author, which appeared in IEICE Trans. Commun. (Japanese Edition), vol.J104-B, no. 3, pp.271–279, Copyright©2021 and IEEE Aerospace Conference 2021, Copyright©2021.
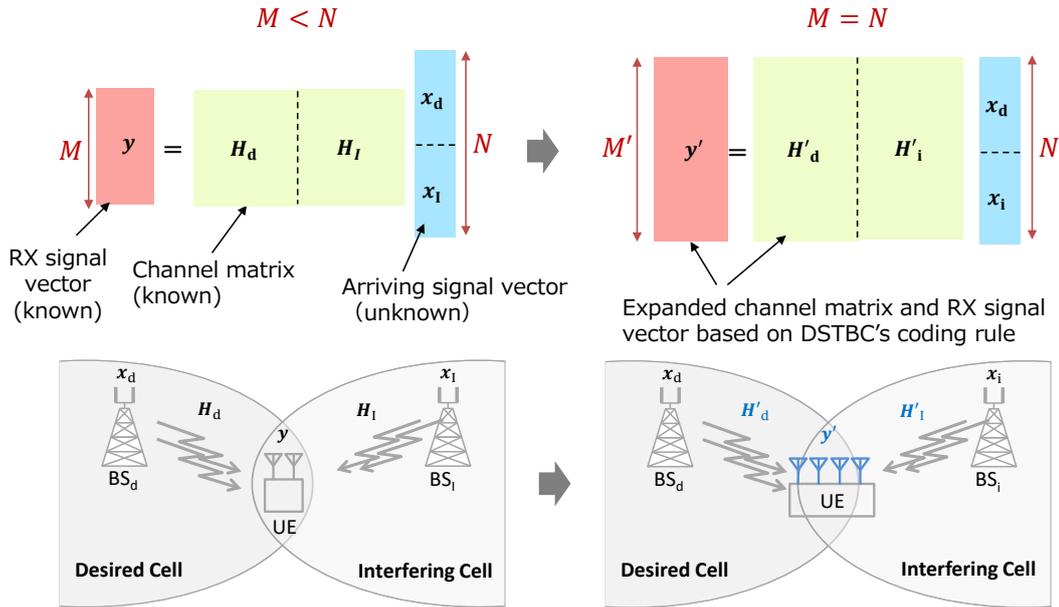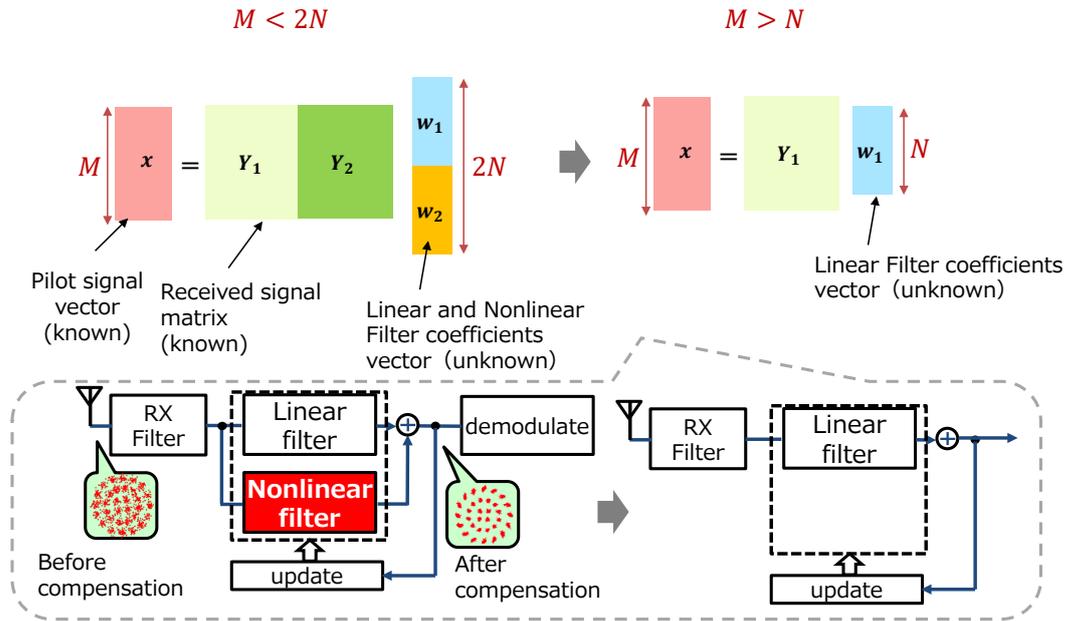
Figure 1.3: Illustration for Chapter 4.

the linear and nonlinear distortions together. However, the proposed equalizer has a larger number of filter coefficients than the conventional linear equalizer. Conventional equalizers use known pilot symbols in the radio frame to estimate the coefficients, but the proposed equalizer cannot directly estimate all the filter coefficients. This is because the number of known pilot symbols is limited in general satellite communication systems such as DVB. Therefore, the proposed equalizer needs to estimate a larger number of filter coefficients than the number of pilot symbols. The proposed method first estimates the coefficients of the linear compensation part with known pilot symbols as in the conventional methods, with the coefficients of the nonlinear compensation part set to 0. Then, it updates both the linear and nonlinear parts' coefficients using a decision-directed LMS (Least Mean Square) algorithm. As a result, all of the filter coefficients are estimated using the same number of known pilot symbols as a conventional linear equalizer. Figure 1.3 shows an illustration of this image.

1.2.4 Successive Interference Cancellation for Asynchronous Signal Collision in Space-based AIS

In Chapter 5[4], the author proposes a novel interference cancellation for space-based AIS.

---

[4]Chapter 5 is based on "Successive Interference Cancellation for Asynchronous Signal Collision in Space-based AIS" [13], by the same author, which appeared in IEEE Aerospace Conference 2022,
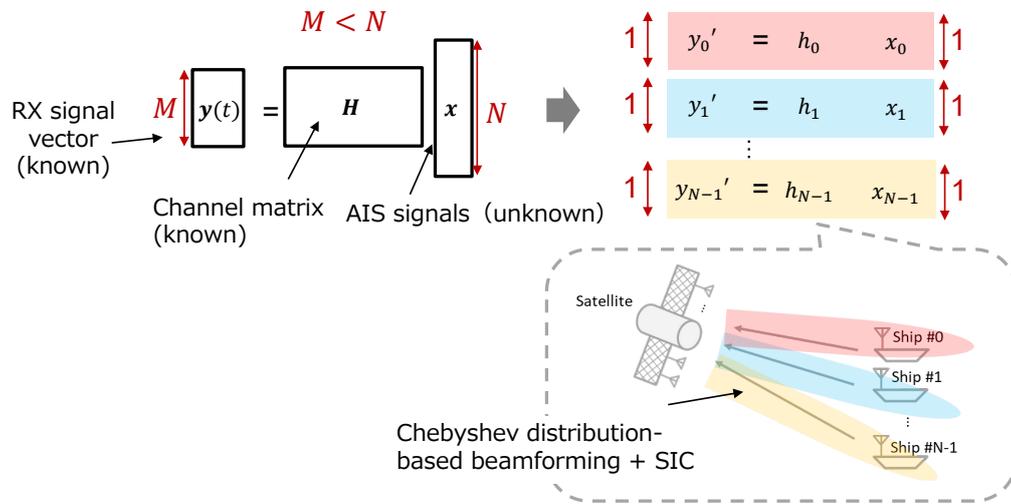
Figure 1.4: Illustration for Chapter 5.

Space-based AIS (Automatic Identification System) is used for global maritime traffic monitoring and safety. In this system, the communication quality deteriorates due to interference by asynchronously colliding AIS signals from multiple ships. Here, when more signals arrive than the number of satellite antennas, it becomes under-determined problem, and these signals cannot be easily separated. Furthermore, since the AIS signals arrive asynchronously and the pilot signals for each AIS signal are same and not orthogonal, it is also difficult to perform channel estimation. In order to suppress this interference and improve the communication quality, this paper proposes a new successive interference cancellation (SIC) scheme combining with beamforming using multiple antennas. In the proposed method, beamforming based on Chebyshev distribution is used to increase the power difference of arriving waves. This separates each interfering signals, and synchronization and demodulation processes are performed for each signal one by one as in the decision problem. Furthermore, SIC reduces the number of unknown signals to deal with the under-determined problem. Figure 1.4 shows an illustration of this image.

Chapter 2

Prediction of Time-Varying Multi-User MIMO Channels Based on DOA Estimation Using Compressed Sensing

This chapter proposes prediction schme of time-varying multi-user MIMO channels based on DOA estimation using compressed sensing.

2.1 Introduction

We may encounter inter-user interference (IUI) and inter-stream interference (IStI) in multi-user multiple-input multiple-output (MIMO) downlink transmission. Block diagonalization (BD) [16] and eigenbeam-space division multiplexing (E-SDM) [17] techniques can be applied to suppress these interferences. To use these techniques, a base station (BS) requires downlink channel state information (CSI) for each user. In time-varying environments, however, MIMO channels change over time because of the motion of user equipment (UEs) and/or surrounding scatterers. Thus, the CSI changes during the time interval between channel estimation and actual signal transmission. This causes interference and deteriorates communication quality.

If we accurately predict channels in such time-varying environments, we can solve the above-mentioned problem and improve communication quality. Channel prediction is important, especially in massive MIMO systems, also known as very large MIMO systems [18]. We have many channels between a BS and UEs in massive MIMO systems and need many training symbols to estimate them. Transmission of many training symbols decreases channel efficiency. Accurate channel prediction can reduce the frequency of the training symbol transmissions and improve channel efficiency.

Channel prediction methods have been extensively investigated in several fields [19]–[32]. We summarize the prediction features for classifying them into three categories. The first one is linear predictors, that is, the autoregressive (AR)-model-based predictor [19], [23] or Wiener predictor [28], [29]. We define the normalized Doppler frequency as the multiplication of the maximum Doppler frequency f_D and prediction time interval τ. The $f_D\tau$ is equal to the spatial prediction range expressed in spatial units: wavelengths[7] [23] and is an important parameter to consider channel predictions. Wang et al. [26] argued that in multi-user MIMO environments, the allowable $f_D\tau$ is less than 0.2. It should be noted that we can only predict MIMO channels within 0.2 wavelengths. In massive MIMO cases, it is up to about 0.05 [28], [29]. The second category involves a polynomial fitting predictor [21], [25]– [27], [31]. The idea is to predict future channels by fitting polynomial curves to measured channels. The predictor does not require channel statistics, such as autocorrelations, and is easy to implement. In the above studies, it was stated that the prediction range is up to about 0.1 or 0.2 depending on the situation. The third category involves the sum-of-sinusoids (SOS) method [22], [24], [30]. This method predicts channels by resolving an arrival signal to a UE into individual multipath components and summing the predicted ones. If the Doppler frequency and complex amplitude of each multipath component are estimated accurately, we can predict reliable channels for a long prediction range. The SOS method is thus promising. The methods discussed in the above references, however, require many training symbols to estimate the Doppler frequencies and complex amplitudes. This is not preferable because of the decrease in channel efficiency. In massive MIMO systems, we should avoid this problem. In this paper, we propose a channel prediction method based on the SOS method using fewer training symbols.

In future mobile communications, higher frequency bands, such as millimeter waves, will be used to transmit a huge amount of information [33]. It is considered that a UE can have many antennas because a wavelength is short in higher frequency bands, and the physical array size is small. We previously proposed an SOS channel prediction method under the assumption that a UE has an array with many antennas [14], [15], [34]– [39]. This channel prediction method resolves an arrival signal to a UE by estimating the direction-of-arrival (DOA) of each multipath component with a compressed sensing technique [3]. In a multi-user MIMO system, this method greatly improves communication quality [40]. However, it is assumed with this method that only the UE moves, and the scatterers surrounding the UE are stationary. The performance of the method deteriorates when this assumption does not hold.

Our SOS channel prediction method uses 2-step compressed sensing without the above assumption. In the first step, we estimate the DOAs using the compressed sensing technique. We improve the estimation accuracy with Khatri-Rao processing [41]. Several

---

[7]Let l and v denote the spatial prediction range and velocity of a UE, respectively. Then, $l = v\tau$ holds. Also, we have $f_D = v/\lambda$, where λ is a wavelength. Thus, $f_D\tau = l/\lambda$ holds. This means that $f_D\tau$ is the spatial prediction range expressed in spatial units: wavelengths.

DOA estimation methods have been presented. The performance of the basic beamforming method is, however, poor because of higher sidelobe levels. The Capon method [42] and subspace methods such as MUSIC [43] and ESPRIT [44], do not work in this situation because the multipath components are coherent, and these methods require the number of arrival waves in advance. Maximum likelihood DOA estimation methods, such as SAGE [45], have a drawback in that the estimation algorithms require appropriate initial values. Compressed sensing does not have the above problems and is promising for DOA estimation. In the second step, we estimate the Doppler frequencies and complex amplitudes for all multipath components by applying compressed sensing again using the estimated DOA information obtained at the first step. The process is done for the channel between a single BS antenna and all UE antennas. For the remaining BS antennas, we calculate the complex amplitudes of the multipath components using the least squares method with less computational complexity. Up to this point, we have estimated the Doppler frequencies and complex amplitudes of the multipath components to the UE antennas from all BS antennas. Using these values, we predict the MIMO channels at the actual transmission time. We evaluated the performance of the proposed channel prediction method in a multi-user MIMO system.

This paper is organized as follows. In Section 2.2, we describe the basic formulation of SOS channel prediction. In Section 2.3, we explain the DOA estimation of the multipath components using first-step compressed sensing. In Section 2.4, we discuss the estimation method of Doppler frequencies and complex amplitudes using second-step compressed sensing. After that, we discuss our channel prediction method. In Section 2.5, we explain the application of the proposed method to a multi-user MIMO system. In Section 2.6, we discuss the evaluation of the proposed method in a multi-user MIMO system. Finally, we conclude the paper in Section 2.7.

2.2 Formulation of SOS Channel Prediction

Let us consider downlink channels. In mobile communication, a signal received at a UE antenna is the summation of multipath components. Note that we assume a narrowband system in which we can ignore the delay between multipath components. The considerations below, however, also hold for each subcarrier of OFDM in a broadband system. In a narrowband system, we cannot resolve the arrival signal into multipath components in the delay domain, and we resolve it estimating the DOAs. For the estimation, we use the sparsity in the spatial domain.

A time-varying channel $h(t)$ at a reference point of a UE array from a certain BS antenna is given by

$$h(t) = \sum_{n=1}^{N} A_n \exp\{j(2\pi f_n t + \phi_n)\},$$ (2.1)

where N denotes the number of multipath components. Also A_n, ϕ_n, and f_n denote the amplitude, phase, and Doppler frequency for the nth multipath component, respectively [23]. From (2.1), if we obtain the complex amplitudes at time $t = 0$: $A_n \exp(j\phi_n)$ and the Doppler frequencies f_n for all the multipath components, we can predict future channels for the UE by summing the predicted multipath components.

In SOS prediction, we need to resolve the signal into multipath components and obtain the Doppler frequencies and complex amplitudes. This is the most important issue with the SOS prediction; therefore, several methods have been proposed [22]– [24], [30]. As stated in detail in the following section, we resolve the signal by estimating the DOAs with first-step compressed sensing. After that, we estimate the Doppler frequencies and complex amplitudes with second-step compressed sensing using the estimated DOA information.

2.3 DOA Estimation Using Compressed Sensing

2.3.1 Compressed Sensing Technique

Compressed sensing is a signal processing technique to reconstruct high-dimensional sparse (most of the elements are 0) signals from fewer measurements and has attracted much attention in many fields. Quantitatively speaking, when we know in advance that true solutions are sparse signals, compressed sensing solves the following simultaneous equations:

$$\mathbf{v} = \mathbf{C}\mathbf{u}. \tag{2.2}$$

Here, $\mathbf{v}$ denotes an M-dimensional observation vector (known), $\mathbf{C}$ is an $M \times K$ observation matrix (known), $\mathbf{u}$ denotes a K-dimensional original signal vector (unknown), and $K > M$ holds. In the above situation, we cannot uniquely reconstruct vector $\mathbf{u}$ from vector $\mathbf{v}$. When $\mathbf{u}$ is sparse, however, we can reconstruct $\mathbf{u}$ using the compressed sensing technique.

There are many algorithms for sparse signal recovery with compressed sensing [4]. In this study, we used the half-quadratic regularization (HQR) method for reconstructing the original signal vector $\mathbf{u}$ since it has been extensively examined for DOA estimation [3]. In the next subsection, we explain how to estimate DOA using the compressed sensing technique.

2.3.2 DOA Estimation

We assume that UEs have a uniform circular array (UCA) with M omnidirectional antennas and that the center of the UCA is the reference point, which is the origin (0,0) in the coordinate system. We also assume that the UEs move at a constant speed and the number of arrival multipath components is expressed as N. The complex amplitude $v_m(t)$ observed at the mth UE antenna whose coordinate is (x_m, y_m) is given by

$$v_m(t) = \sum_{n=1}^{N} b_n(t) \, \mathrm{e}^{j\frac{2\pi}{\lambda}(x_m \cos\psi_n + y_m \sin\psi_n)}, \tag{2.3}$$
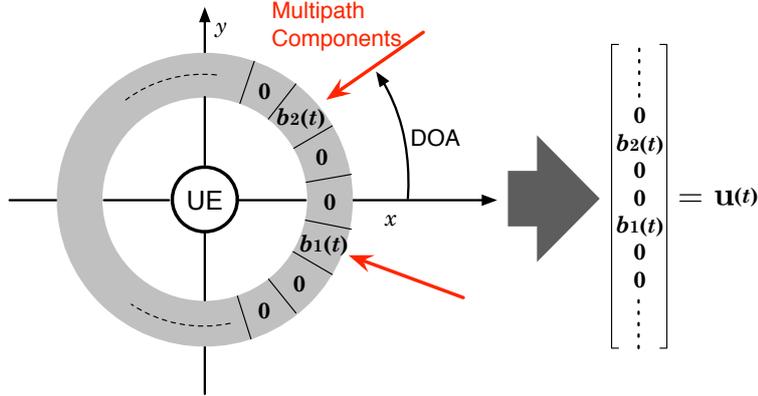
Figure 2.1: Formulation of original signal vector. Reprinted from [9] with permission (©2019 IEEE).

where $b_n(t)$ and ψ_n denote the complex amplitude at the reference point at time t and the DOA of the nth multipath component, respectively. Because the DOAs of multipath components change relatively slowly [46], we can assume that they are constant for the channel prediction period. Here, $b_n(t)$ includes the effect of the phase rotation by the Doppler frequency, as explained in Sec. 2.4. Also, λ denotes the wavelength for the center frequency. The $v_m(t)$ can be observed using pilot symbols, although thermal noise is included. Using these observed signals, we can estimate the number of arrivals N, DOAs ψ_n, and complex amplitudes $b_n(t)$ ($n = 1, 2, \cdots, N$) with compressed sensing technique, as stated below.

As shown in Fig. 2.1, we assume that a UE is located on the origin of coordinates and divide the angle space surrounding the UE into K small bins, which are shown on the gray ring. If the nth multipath component arrives in the direction corresponding to a bin, the value for the bin is the complex amplitude $b_n(t)$. The bins have the value of 0 when no multipath component arrives in the corresponding direction. We express the original signal vector $\mathbf{u}(t)$ as shown on the right side in Fig. 2.1. The $\mathbf{u}(t)$ is reconstructed using signals received at the UE antenna array. This can be done by compressed sensing. Once $\mathbf{u}(t)$ is reconstructed, the DOAs and complex amplitudes of all the multipath components are obtained. We express the angle of the kth bin as ψ'_k and the estimated complex amplitude of the multipath component from ψ'_k at the origin as $u_k(t)$. Note that if a multipath component does not arrive from ψ'_k, we have $u_k(t) = 0$. We represent the observation vector $\mathbf{v}(t)$, original signal vector $\mathbf{u}(t)$, and thermal noise vector $\mathbf{n}(t)$ as

$$\mathbf{v}(t) = [v_1(t), v_2, (t) \ldots, v_M(t)]^{\mathrm{T}} \tag{2.4}$$

$$\mathbf{u}(t) = [u_1(t), u_2(t), \ldots, u_K(t)]^{\mathrm{T}} \tag{2.5}$$

$$\mathbf{n}(t) = [n_1(t), n_2(t), \ldots, n_M(t)]^{\mathrm{T}}, \tag{2.6}$$

where $[\cdot]^{\mathrm{T}}$ denotes transpose. From (2.3), the (m, k)th element of the observation matrix

C is written as

$$e^{j\frac{2\pi}{\lambda}(x_m \cos \psi'_k + y_m \sin \psi'_k)}. \tag{2.7}$$

From the above,

$$\mathbf{v}(t) = \mathbf{C}\mathbf{u}(t) + \mathbf{n}(t) \tag{2.8}$$

holds. If $N \ll K$, viz., the number of arrival multipath components is much smaller than that of the bins, we can consider that the original signal vector $\mathbf{u}(t)$ is sparse.

We use a channel prediction method for a higher frequency band such as 20 GHz. According to Akdeniz et al. [46], who derived channel models based on the measurements at 28 and 73 GHz, there are few clusters at such higher frequency bands. Although UE cluster root-mean-squared (rms) angular spreads are wider than BS ones in the azimuth direction, the difference is small. From each cluster, many multipath components, called subpaths [46] or rays [47], arrive at a UE. They are distributed according to the wrapped Gaussian probability density function (pdf) [46] or the truncated Laplacian pdf [47]. In either case, we can see that most of the subpaths are distributed around the center of each cluster, and that their arrival angles are close. Consequently, they have approximately the same Doppler frequencies, and we treat all the subpaths from a common cluster as a single multipath component. In this case, the nth multipath component in (2.1) corresponds to the signal from the nth cluster. From these results, it is conjectured that we can assume sparsity at a UE side, and that $N \ll K$ holds. If we assume a ring of scatterers surrounding each UE, the scatterers do not exist continuously or densely on the ring, but we have few discrete scatterers on it. Thus, we can apply compressed sensing to (2.8) and estimate the number of multipath components N, the DOAs ψ_n, and the complex amplitudes $b_n(t)$.

Because we treat the subpaths with slightly different Doppler frequencies from a common cluster as a single multipath component, $A_n \exp(j\phi_n)$ in (2.1) is slowly time-varying, and the prediction accuracy will degrade. Our goal in this paper is, however, to propose a prediction method using 2-step compressed sensing and show the basic performance of the method. Performance analysis taking the exact Doppler frequencies of the subpaths into account is for future work.

2.3.3   DOA Estimation Using Khatri-Rao Processing

As stated in the previous subsection, there are few multipath components, and multipath environments are sparse. However, it is preferable if we can treat many multipath components at a UE because this is more reliable. In higher frequency bands, a UE can have many antennas. The number of antennas M is, nevertheless, limited. The performance of DOA estimation with compressed sensing deteriorates when the number of multipath components increases. In this subsection, we introduce Khatri-Rao processing [41] to overcome this problem. This processing can improve DOA estimation accuracy. Moreover, the estimation accuracy does not depend on the phase change of arrival multipath components

because the original signal vector $\mathbf{u}(t)$ does not consist of complex amplitudes but of the powers in this processing.

The correlation matrix at time t of the observation vector $\mathbf{v}(t)$ is given by

$$\mathbf{R}^{(\mathrm{S})}(t) = \mathrm{E}[\mathbf{v}(t)\mathbf{v}^{\mathrm{H}}(t)] = \mathbf{C}\mathbf{S}(t)\mathbf{C}^{\mathrm{H}} + \mathbf{R}_N^{(\mathrm{S})}(t), \tag{2.9}$$

where $\mathrm{E}[\cdot]$ denotes the ensemble averaging, $^{\mathrm{H}}$ the Hermitian conjugate, $\mathbf{S}(t)$ the multipath component correlation matrix at time t, and $\mathbf{R}_N^{(\mathrm{S})}(t)$ the noise correlation matrix at time t. With Khatri-Rao processing, it is assumed that the arrival multipath components are uncorrelated, viz., $\mathbf{S}(t)$ is the diagonal matrix. Thus, if the arrival waves are coherent, DOA estimation using Khatri-Rao processing deteriorates [48]. We explain how to solve this problem in the next subsection.

When $\mathbf{S}(t)$ is the diagonal matrix, the following equation holds:

$$\begin{aligned} \mathrm{vec}(\mathbf{R}^{(\mathrm{S})}(t)) &= \mathrm{vec}(\mathbf{C}\mathbf{S}(t)\mathbf{C}^{\mathrm{H}}) + \mathrm{vec}(\mathbf{R}_N^{(\mathrm{S})}(t)) \\ &= (\mathbf{C}^* \odot \mathbf{C})\tilde{\mathbf{u}}(t) + \mathrm{vec}(\mathbf{R}_N^{(\mathrm{S})}(t)). \end{aligned} \tag{2.10}$$

Here, * is the complex conjugate, $\odot$ is the operator of the Khatri-Rao product [41], $\mathrm{vec}(\cdot)$ is the operator to transform a matrix into a vector, and $\tilde{\mathbf{u}}(t)$ is the K-dimensional column vector consisting of the diagonal elements of $\mathbf{S}(t)$. Note that $\tilde{\mathbf{u}}(t)$ is a sparse vector. This is the same as in (2.5), but $\tilde{\mathbf{u}}(t)$ does not consist of complex amplitudes but powers.

Here, we define the following vectors and matrix:

$$\tilde{\mathbf{v}}(t) = \mathrm{vec}(\mathbf{R}^{(\mathrm{S})}(t)) \tag{2.11}$$

$$\tilde{\mathbf{C}} = \mathbf{C}^* \odot \mathbf{C} \tag{2.12}$$

$$\tilde{\mathbf{n}}(t) = \mathrm{vec}(\mathbf{R}_N^{(\mathrm{S})}(t)). \tag{2.13}$$

Using the above equations, we can rewrite (10) as

$$\tilde{\mathbf{v}}(t) = \tilde{\mathbf{C}}\tilde{\mathbf{u}}(t) + \tilde{\mathbf{n}}(t). \tag{2.14}$$

Also in the above equation, $\tilde{\mathbf{u}}(t)$ is sparse; thus, we can apply compressed sensing to (2.14). It should be noted that the dimension of $\tilde{\mathbf{v}}(t)$ is M^2 and is larger than that of $\mathbf{v}(t)$ in (2.8): M. This is the reason Khatri-Rao processing can improve DOA estimation accuracy.

Next, we discuss further improvement of DOA estimation accuracy using the fact that the elements of $\tilde{\mathbf{u}}(t)$ are powers. Here, L denotes the number of antennas at the BS. As seen from Fig. 2.2, the number of multipath components and the DOAs to the UE are the same for all BS antennas. Also, the powers of the arrival multipath components are the same, and we can write the observation vector $\tilde{\mathbf{v}}_j(t)$ obtained with the pilots from the BS antenna #j as

$$\tilde{\mathbf{v}}_j(t) = \tilde{\mathbf{C}}\tilde{\mathbf{u}}(t) + \tilde{\mathbf{n}}_j(t) \qquad (j = 1, 2, \cdots, L). \tag{2.15}$$

Averaging the above L equations, we have

$$\tilde{\mathbf{v}}_{\mathrm{MEAN}}(t) = \tilde{\mathbf{C}}\tilde{\mathbf{u}}(t) + \tilde{\mathbf{n}}_{\mathrm{MEAN}}(t), \tag{2.16}$$
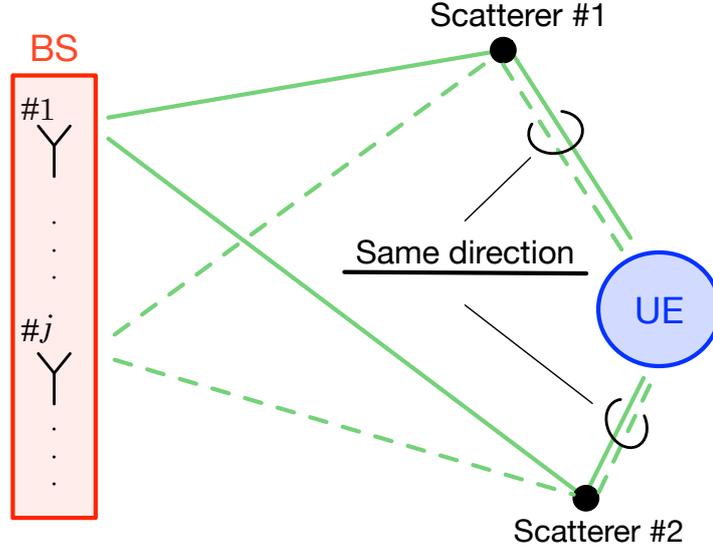
Figure 2.2: Multipath components from multiple antennas at BS. Reprinted from [9] with permission (©2019 IEEE).

where $\tilde{\mathbf{v}}_{\text{MEAN}}(t)$ and $\tilde{\mathbf{n}}_{\text{MEAN}}(t)$ are given by

$$\tilde{\mathbf{v}}_{\text{MEAN}}(t) = \frac{1}{L} \sum_{j=1}^{L} \tilde{\mathbf{v}}_j(t) \tag{2.17}$$

$$\tilde{\mathbf{n}}_{\text{MEAN}}(t) = \frac{1}{L} \sum_{j=1}^{L} \tilde{\mathbf{n}}_j(t). \tag{2.18}$$

The effect of thermal noise decreases due to averaging, and we can estimate the DOAs with higher accuracy using the pilots from all BS antennas.

2.3.4 Decorrelation of Multipath Components Using Motion of UE

As stated in Section 2.2, we assume that the frequency bandwidth of the transmitted signal is so narrow that the delay difference between multipath components is negligibly small compared with the symbol duration. Thus, the arrival multipath components to a UE are perfectly correlated. For example, this holds for each subcarrier in OFDM systems. In this case, (2.10) does not hold. This is because $\mathbf{S}(t)$ is not a diagonal matrix. To solve this problem, we can use spatial smoothing preprocessing (SSP) and decrease almost everywhere the correlations between the arrival multipath components [49].

We assume that we have P sets of observation signals obtained at multiple times $(t = t_1, t_2, \cdots, t_P)$, as shown in Fig. 2.3. The BS transmits the pilot signals at time
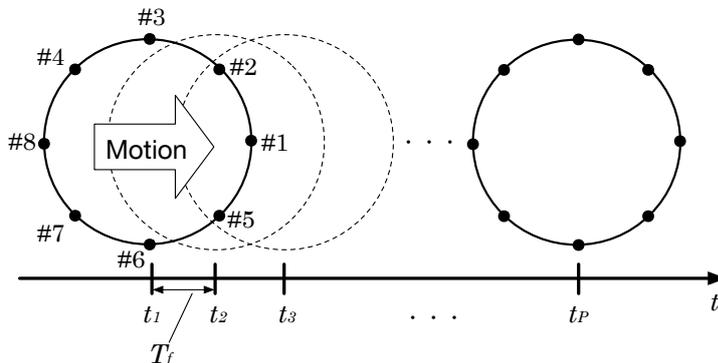
Figure 2.3: Motion of UE and observation at multiple times. Rings represent UCA on UE. Reprinted from [9] with permission (©2019 IEEE).

$t_1, t_2, \cdots, t_P$ with interval (frame duration) T_f, and the UE receives them P times, as shown in Fig. 2.3. We assume that the radio propagation environment (the number of multipath components, the DOAs, and their powers) does not change during the observation period.

We can decrease almost everywhere the correlations between the arrival multipath components by averaging the correlation matrix of the observation vector obtained at time t_p as follows:

$$\mathbf{R}_{\text{SSP}} = \frac{1}{P} \sum_{p=1}^{P} \mathbf{R}^{(\text{S})}(t_p). \tag{2.19}$$

We use the decorrelation method called modified SSP (MSSP) or forward–backward SSP [49] because this method is more effective than SSP. This method can be applied when antenna elements are placed symmetrically with respect to the origin. To meet this condition, we assign an antenna number, as shown in Fig. 2.3. The MSSP uses $\mathbf{R}^{(\text{M})}(t)$ defined as

$$\mathbf{R}^{(\text{M})}(t) = \frac{1}{2} \{ \mathbf{R}^{(\text{S})}(t) + \mathbf{J}(\mathbf{R}^{(\text{S})}(t))^* \mathbf{J} \}, \tag{2.20}$$

where $\mathbf{J}$ is an $M \times M$ exchange matrix defined as follows:

$$\mathbf{J} = \begin{bmatrix} 0 & 0 & \cdots & 0 & 1 \\ 0 & 0 & \cdots & 1 & 0 \\ \vdots & & & & \vdots \\ 0 & 1 & \cdots & 0 & 0 \\ 1 & 0 & \cdots & 0 & 0 \end{bmatrix} \tag{2.21}$$

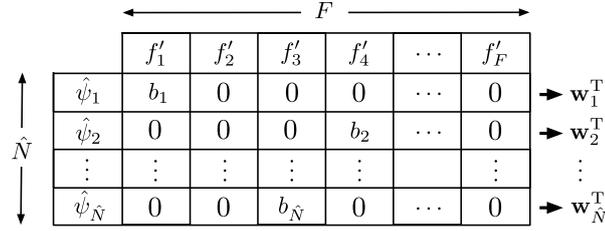|	f'_1	f'_2	f'_3	f'_4	$\cdots$	f'_F	
$\hat{\psi}_1$	b_1	0	0	0	$\cdots$	0	$\mathbf{w}_1^{\mathrm{T}}$
$\hat{\psi}_2$	0	0	0	b_2	$\cdots$	0	$\mathbf{w}_2^{\mathrm{T}}$
$\vdots$	$\vdots$	$\vdots$	$\vdots$	$\vdots$		$\vdots$	$\vdots$
$\hat{\psi}_{\hat{N}}$	0	0	$b_{\hat{N}}$	0	$\cdots$	0	$\mathbf{w}_{\hat{N}}^{\mathrm{T}}$

Figure 2.4: Constitution method of original signal vector for estimating Doppler frequency and complex amplitude. Reprinted from [9] with permission (©2019 IEEE).

As in the case of (2.19), we average $\mathbf{R}^{(\mathrm{M})}(t)$ to reduce the correlations as given by

$$\mathbf{R}_{\mathrm{MSSP}} = \frac{1}{P}\sum_{p=1}^{P}\mathbf{R}^{(\mathrm{M})}(t_p). \tag{2.22}$$

We apply $\mathbf{R}_{\mathrm{MSSP}}$ given by (2.22) to $\mathbf{R}^{(\mathrm{S})}(t)$ in (2.11). After the above preprocessing, we can decrease almost everywhere the correlations and use compressed sensing with Khatri-Rao processing in the current situation. The reduction in the correlations in $\mathbf{R}_{\mathrm{SSP}}$ and $\mathbf{R}_{\mathrm{MSSP}}$ is proved in the Appendix.

2.4 Doppler Frequency and Complex Amplitude Estimation

We express the number of multipath components and their DOAs estimated with the compressed sensing technique stated in the previous section as $\hat{N}$ and $\hat{\psi}_n$ ($n = 1, 2, \cdots, \hat{N}$), respectively. In this section, we describe how to estimate the Doppler frequencies and complex amplitudes by applying second-step compressed sensing. In (2.3), we express the complex amplitude of the nth multipath component at time t as $b_n(t)$. Using the Doppler frequency f_n, we can write $b_n(t) = b_n e^{j2\pi f_n t}$. Note that b_n is the complex amplitude of the nth multipath component at time $t = 0$. From the above expression, we can rewrite (2.3) as

$$v_m(t) = \sum_{n=1}^{N} b_n\, e^{j\frac{2\pi}{\lambda}(x_m\cos\psi_n + y_m\sin\psi_n)} \cdot e^{j2\pi f_n t}. \tag{2.23}$$

2.4.1 Formulation of Doppler Frequency and Complex Amplitude Estimation

We assume that the Doppler frequencies exist from $-f_D$ to f_D. We separate the range into F small bins. We express the Doppler frequency at the ith bin as f'_i ($i = 1, 2, \cdots, F$). As shown in Fig. 2.4, we consider the $\hat{N} \times F$ matrix whose elements are the complex amplitudes of arrival multipath components. When the Doppler frequency of the multipath component from direction $\hat{\psi}_n$ is equal to f'_i, the (n, i)th element has the complex amplitude b_n. We express the F-dimensional original signal vector for the multipath component arriving from $\hat{\psi}_n$ as $\mathbf{w}_n$ and define the $\hat{N}F$-dimensional original signal vector $\mathbf{w}$ as

$$\mathbf{w} = [\mathbf{w}_1^{\mathrm{T}}, \, \mathbf{w}_2^{\mathrm{T}}, \ldots, \, \mathbf{w}_{\hat{N}}^{\mathrm{T}}]^{\mathrm{T}}. \tag{2.24}$$

Also in the above equation, it is clear that the original signal vector $\mathbf{w}$ is sparse, and we can apply compressed sensing to (2.24).

Next, we consider the observation vector and observation matrix to reconstruct $\mathbf{w}$. Also in this case, we use the observation vector $\mathbf{v}(t)$ defined with (2.4). We introduce the $M \times F\hat{N}$ observation matrix as $\mathbf{C}'(t)$ that satisfies the following equation

$$\mathbf{v}(t) = \mathbf{C}'(t)\mathbf{w} + \mathbf{n}(t). \tag{2.25}$$

We define the F-dimensional row vector $\mathbf{c}'^{(m)}_n$ as

$$\mathbf{c}'^{(m)}_n = \left[\begin{array}{c} e^{j\frac{2\pi}{\lambda}(x_m \cos \hat{\psi}_n + y_m \sin \hat{\psi}_n)} \cdot e^{j 2\pi f'_1 t} \\ e^{j\frac{2\pi}{\lambda}(x_m \cos \hat{\psi}_n + y_m \sin \hat{\psi}_n)} \cdot e^{j 2\pi f'_2 t} \\ \vdots \\ e^{j\frac{2\pi}{\lambda}(x_m \cos \hat{\psi}_n + y_m \sin \hat{\psi}_n)} \cdot e^{j 2\pi f'_F t} \end{array} \right]^{\mathrm{T}}. \tag{2.26}$$

The (m, n)th, $(m, n + 1)$th, $\cdots$, $(m, n + F - 1)$th elements of $\mathbf{C}'(t)$ correspond to the elements in (2.26).

As shown in Fig. 2.3, we have P sets of observation data and can derive the following equation

$$\bar{\mathbf{v}} = \bar{\mathbf{C}}'\mathbf{w} + \bar{\mathbf{n}}, \tag{2.27}$$

where $\bar{\mathbf{v}}$, $\bar{\mathbf{C}}$, and $\bar{\mathbf{n}}$ are defined as

$$\bar{\mathbf{v}} = \left[\mathbf{v}(t_1)^{\mathrm{T}}, \, \mathbf{v}(t_2)^{\mathrm{T}}, \ldots, \, \mathbf{v}(t_P)^{\mathrm{T}} \right]^{\mathrm{T}} \tag{2.28}$$

$$\bar{\mathbf{C}}' = \left[\mathbf{C}'(t_1)^{\mathrm{T}}, \, \mathbf{C}'(t_2)^{\mathrm{T}}, \ldots, \, \mathbf{C}'(t_P)^{\mathrm{T}} \right]^{\mathrm{T}} \tag{2.29}$$

$$\bar{\mathbf{n}} = \left[\mathbf{n}(t_1)^{\mathrm{T}}, \, \mathbf{n}(t_2)^{\mathrm{T}}, \ldots, \, \mathbf{n}(t_P)^{\mathrm{T}} \right]^{\mathrm{T}}. \tag{2.30}$$

From (2.27), we can reconstruct $\mathbf{w}$ with compressed sensing and obtain the Doppler frequencies and complex amplitudes for all the multipath components.

2.4.2 Avoidance of Ambiguity in Doppler Frequency Estimation

When phases of multipath components rotate by larger than π during the time interval T_f in channel estimation, we have ambiguity in Doppler frequency estimation described in the previous subsection. We assume that the BS transmits the pilot signals with T_f, and the UE observes them, as shown in Fig. 2.3. To avoid this ambiguity, the BS transmits the pilot signals also at time t_1' between t_1 and t_2. We set t_1' in such a way that the period $t_1' - t_1$ is so short that the phase rotation during that period does not exceed π. We include the observation data at t_1' in (2.28) and modify (2.27) and (2.29). From this modification, we can avoid phase ambiguity and correctly estimate the Doppler frequencies, even when the phases rotate by larger than π during the time interval T_f.

2.4.3 Channel Prediction Values at UE Antennas

The estimated multipath values stated above are for the reference point of the UE. We need to transform those values to those at each UE antenna. These values can be calculated considering the phase rotation due to the path difference between the reference point and each UE antenna. Furthermore, considering the phase rotation $\mathrm{e}^{j2\pi \hat{f}_n \tau}$ due to the Doppler shifts, we can obtain the channel prediction value $\hat{h}_m(\tau)$ for the mth UE antenna at future time $t = \tau$. That is, applying the estimated Doppler frequencies and complex amplitudes to (2.23), we have

$$\hat{h}_m(\tau) = \sum_{n=1}^{\hat{N}} \hat{b}_n \, \mathrm{e}^{j \frac{2\pi}{\lambda}(x_m \cos \hat{\psi}_n + y_m \sin \hat{\psi}_n)} \cdot \mathrm{e}^{j2\pi \hat{f}_n \tau}. \tag{2.31}$$

2.5 Application to MIMO system

In the previous sections, we discussed the channels between a single BS antenna and all UE antennas. In MIMO systems, we also have multiple antennas at the BS. We need to predict all the channels between the BS antennas and UE ones. Application of the compressed sensing technique to all the MIMO channels, however, requires huge computational complexity. In this section, we discuss our proposed channel prediction method of estimating the complex amplitudes of the multipath components for all BS antennas with lower computational burden.

We assume that we have obtained the channels between BS antenna #1 and the UE antennas using the compressed sensing technique. As seen from Fig. 2.2, the number of multipath components, the DOAs, and the Doppler frequencies are the same for all BS antennas and were obtained using BS antenna #1. Thus, we need to obtain only the complex amplitudes of the multipath components from BS antennas #j ($j = 2, 3, \cdots, L$). Figure 2.5(a) shows the schematic expression of the linear measurement (2.27) except the noise term $\bar{\mathbf{n}}$ for BS antenna #1. The gray parts in $\mathbf{w}$ indicate non-zero elements, and the gray ones in $\bar{\mathbf{C}}'$ indicate the columns corresponding to the non-zero elements in $\mathbf{w}$.
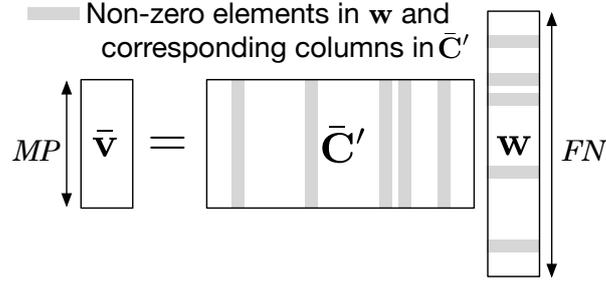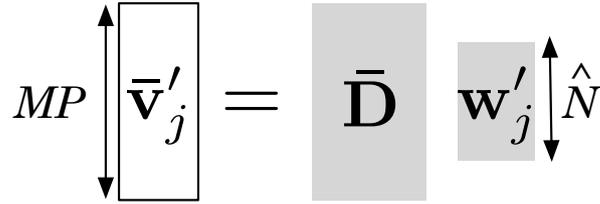
(a) Equation (2.27) except $\bar{\mathbf{n}}$ for BS antenna #1

(b) Equation for BS antenna #j ($j = 2, 3, \cdots, L$)

Figure 2.5: Schematic expressions of linear measurements. Reprinted from [9] with permission ((C)2019 IEEE).

We introduce the $\hat{N}$-dimensional vector $\mathbf{w}'_j$ deleting the zero elements in $\mathbf{w}$, as shown in Fig. 2.5(b). We also introduce the $MP \times \hat{N}$ matrix $\bar{\mathbf{D}}$ deleting the columns in $\bar{\mathbf{C}}'$, which correspond to the zero elements in $\mathbf{w}$. From the above, the MP-dimensional observation vector $\bar{\mathbf{v}}'_j$ for BS antenna #j is given by

$$\bar{\mathbf{v}}'_j = \bar{\mathbf{D}}\mathbf{w}'_j + \bar{\mathbf{n}}'_j, \tag{2.32}$$

where $\bar{\mathbf{n}}'_j$ denotes the MP-dimensional noise vector for BS antenna #j. Equation (2.32) is different from the compressed sensing problem given by (2.27). We set the values of MP in such a way that $MP > \hat{N}$ holds. Thus, we can easily solve (2.32) using the least squares method as follows:

$$\mathbf{w}'_j = (\bar{\mathbf{D}}^{\mathrm{H}}\bar{\mathbf{D}})^{-1}\bar{\mathbf{D}}^{\mathrm{H}}\bar{\mathbf{v}}'_j. \tag{2.33}$$

By applying the above processing to BS antennas #j ($j = 2, 3, \cdots, L$), we can obtain the complex amplitudes for all BS antennas and predict all MIMO channels from (2.31).

Here, we state the computational complexity of the proposed method. We evaluated it by the number of complex multiplications required at each step. As will be stated in Section 2.6, we assumed that a single pilot symbol was sent from each BS antenna in a frame. The numbers of complex multiplications are given as follows:

1. Data acquisition for Khatri-Rao Processing (2.9), (2.17), (2.22):

$\mathbf{R}^{(S)}(t)$ given by (2.9) is an $M \times M$ matrix and has M^2 elements, but it is a Hermitian matrix. We need only $M(M + 1)/2$ multiplications to obtain $\mathbf{R}^{(S)}(t)$. Then, the required multiplications for the step 1) is $M(M + 1)PL/2$.

2. DOA estimation using the compressed sensing (HQR):

   The procedure of HQR is stated in Subsection 3.2 in [3]. Note that the number of snapshots T in [3] was 1 in our case. Multiplications that do not involve received signals can be carried out in advance, and we do not need to consider their computational burden. The HQR is an iterative method. Before the iterative process, we need M^2K multiplications. At each iteration step, $K^3 + K^2 + 3K + 1$ multiplications and K exponential operations are required. Note that the exponential operation results can be obtained using a lookup table, and the computational load is much lighter than multiplications.

3. Doppler frequency and complex amplitude estimation (second step compressed sensing):

   As the item 2), HQR was used for the estimation, and T in [3] was 1 also in this case. Before the iterative process, we need $M(P + 1)F\hat{N}$ multiplications. Each iteration step involves $(F\hat{N})^3 + (F\hat{N})^2 + 3F\hat{N} + 1$ multiplications and $F\hat{N}$ exponential operations. We can obtain the exponential operation results using a lookup table.

4. Complex amplitude estimation for the remaining $(L - 1)$ BS antennas (2.33):

   The number of mutiplications is $(L - 1)(MP + \hat{N})\hat{N}(\hat{N} + 1)$.

5. If OFDM is used for the MIMO transmission, the above processing is for one of the subcarriers. For the other subcarriers, we do not need the steps 1) to 3) because the DOAs and Doppler frequencies are the same and have been obtained. Thus, we need only the complex amplitudes given by (2.33) for the L BS antennas, and the number of complex multiplications for each subcarrier is $L(MP + \hat{N})\hat{N}(\hat{N} + 1)$.

2.6   Simulations

We evaluated the performance of the proposed channel prediction method in a time-varying three-user MIMO downlink system. We assumed the frequency-flat fading environment, which follows Jakes' model. The simulation parameters are listed in Table 2.1. In this paper, we do not consider a specific system to which we apply the proposed method. A center frequency of 20 GHz is just an example in a higher frequency band. The BS used the transmit precoding matrix combining the BD and E-SDM techniques. The data rate for each UE was fixed constantly at 8 bits/symbol. Thus, we had the following five transmission patterns:

(a. single-stream transmission of 256 QAM

(b. two-stream transmission of 64 QAM and QPSK

(c. two-stream transmission of 16 QAM

(d. single-stream transmission of 16 QAM and two-stream transmission of QPSK

(e. four-stream transmission of QPSK

The resource control for the E-SDM transmission, viz., determining the number of streams, modulation scheme, and transmit power, was done in such a way that the Chernoff upper bound of the bit error rate (BER) for each UE was the lowest [17]. The total transmit (TX) power per user was the same, and error correction codes were not used. Each UE determined the MMSE weights using its own effective downlink channels. Thus, the UEs suppressed IStI for multiple-stream transmission; however, they did not suppress IUI. Furthermore, we took channel estimation errors into account for realistic evaluation. Multi-user MIMO systems require two types of channels: (i) downlink channels to determine TX weights at the BS and (ii) effective downlink channels including the effects of TX weights to determine the receive (RX) weights at the UEs. We estimated these channels using pilot symbols. The estimated values contained errors due to thermal noise. We assumed a single unweighted pilot symbol from each TX antenna in a frame for the downlink channels (i) and a single weighted pilot symbol for the effective downlink channels (ii). Using a single pilot symbol per TX antenna corresponds to "No. of snapshots 1" in Table 2.1. We also assumed that all pilot symbols were transmitted separately in the time domain. Note that we did not have interference from other antennas in the pilot symbol transmission period.

In the proposed method, we need the vector $\tilde{\mathbf{v}}_{\mathrm{MEAN}}(t)$ for Khatri-Rao processing, which is defined by (2.17). The vector $\tilde{\mathbf{v}}_j(t)$ is transformed from the correlation matrix, as in (2.11). Both the correlation matrix and vector are statistical quantities. They were calculated with the unweighted pilot symbols. We have L antennas at the BS. Also, as stated in Section 2.3, we have P frames for the MSSP. Thus, we have LP samples to obtain the vector $\tilde{\mathbf{v}}_{\mathrm{MEAN}}(t)$. Because L was 24, we had 72, 96, or 120 samples for averaging depending on P that had the value of 3, 4, or 5.

As seen from the above, the pilots needed for the proposed channel prediction method is P unweighted symbols per TX antenna and an additional single one. The latter is sent from an arbitrary TX antenna to avoid ambiguity in the Doppler frequency estimation, as stated in subsection 2.4.2. It is seen that the proposed method does not require many pilot symbols.

2.6.1 Jakes' model

We used Jakes' model in the simulations. As shown in Fig. 2.6, the BS was placed at the origin, and UE1, UE2, and UE3 were located at $-\pi/4, \pi/4$, and $3\pi/4$ from the x-axis, respectively. We assumed nine scatterers uniformly distributed on a ring surrounding each UE, and the angle spread from the BS to each ring of scatterers was equal to $\pi/3$. Figure 2.7 shows the configuration of the BS and UE arrays, and the multipath components to the

Table 2.1: Simulation Parameters

	No. of users	3
	No. of BS & UE antennas	24 x 8
	Data rate	8 bits/symbol/user
	Modulation schemes	QPSK, 16QAM, 64QAM, 256QAM
	Resource control	Minimum BER criterion based on Chernoff upper bound [17]
	Data burst length	128 symbols
	Frame duration (T_f)	5 ms
	$t'_1 - t_1$	1 ms
	Center frequency (f_c)	20 GHz
	Maximum Doppler frequency (f_D)	200 Hz
	Thermal noise	Additive white Gaussian noise
	Precoding	BD + E-SDM
	RX signal processing at UE	MMSE weighting
	No. of scatterers (multipath components)	9
	No. of bins (K) for DOA estimation	360 (1° interval)
	No. of bins (F) for Doppler frequency estimation	201 (2 Hz interval)
	No. of snapshots	1
	Parameters of HQR method [3]	
α		10 (DOA estimation) 0.1 (Doppler Frequency and complex amplitude estimation)
ϵ		1.0×10^{-5}
p		0.001 (DOA estimation) 0.1 (Doppler Frequency and complex amplitude estimation)
δ		1.0×10^{-6}

UE. Omnidirectional TX antennas with half-wavelength spacing at 20 GHz were aligned along the y-axis at the BS, and the UEs had an eight-element UCA whose radius was a wavelength. The MIMO channels were uncorrelated regarding different UEs because the scatterers were different. As for the same UE, the correlations of channels ranged from almost 0 to about 0.7.

As stated previously, the UEs moved at a constant speed (1.5 m/s). The scatterers moved at a constant speed that was distributed independently and uniformly in the range from 0 to 1.5 m/s. Also, the moving directions of the UEs and scatterers were uniformly random from 0 to 2π.
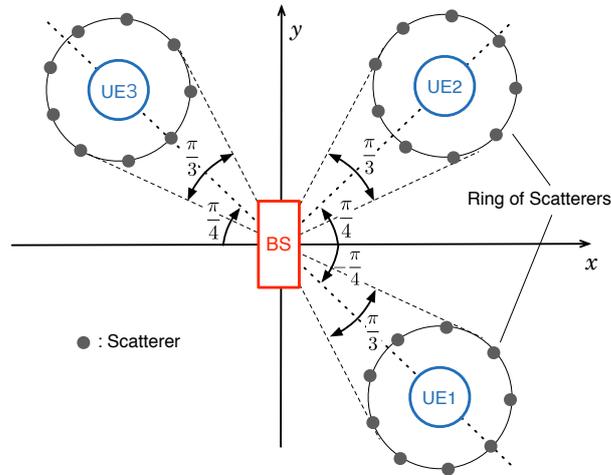
Figure 2.6: Positions of BS and UEs in Jakes' environment. Reprinted from [9] with permission (©2019 IEEE).
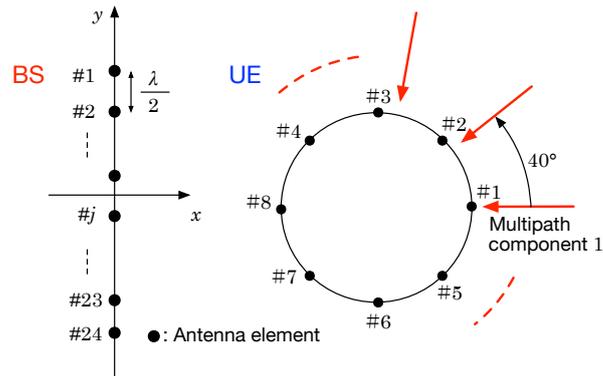

Figure 2.7: Configuration of arrays and arrival multipath components to UE. Reprinted from [9] with permission (©2019 IEEE).

2.6.2 Analyses of performance

Figure 2.8 plots a cumulative distribution of relative channel prediction error for #1 antenna at UE1 in the following cases:

(i. the proposed channel prediction method for $P = 3 \sim 5$ (2-step CS Prediction)

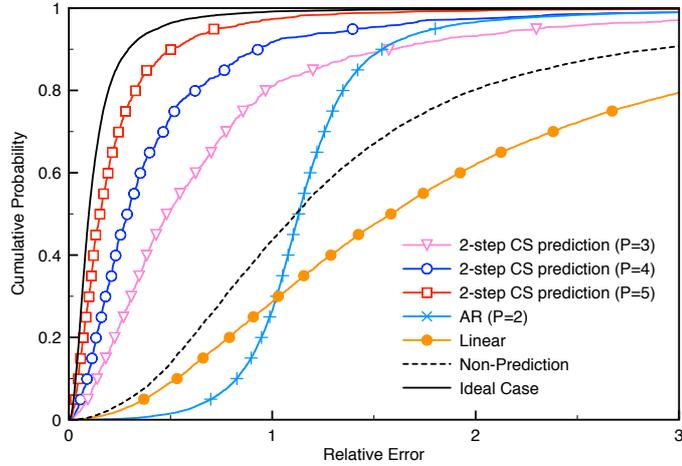(ii. the AR-model-based channel prediction method with the order two (AR ($P = 2$))
[27]

Figure 2.8: Cumulative probability of relative channel prediction error. Reprinted from [9] with permission (©2019 IEEE).

(iii. the channel prediction method using the simple linear extrapolation (Linear) [27]

(iv. channel prediction was not done (Non-Prediction)

(v. the UE and scatterers were stationary ($f_D = 0$) (Ideal Case). Note that although we have no prediction error, we have estimation error due to noise.

The relative channel prediction error is calculated as follows:

$$\frac{|\hat{h} - h|}{|h|},\tag{2.34}$$

where $\hat{h}$ denotes the predicted channel and h denotes the actual channel. Except for case (v), we assumed a maximum Doppler frequency f_D of 200 Hz, which corresponded to the velocity of a UE and scatter of 1.5 m/s, and the center frequency f_c of 20 GHz. Note that the maximum relative velocity was 3.0 m/s because both the UEs and scatterers moved. Also, the time τ from the channel estimation was 2.5 ms ($T_f/2$). In this figure, the normalized TX power was 20 dB. The normalized TX power is defined as the TX power per UE normalized by the value yielding the average SNR of 0 dB at the single omnidirectional antenna receiver when a signal is transmitted from the single omnidirectional antenna. For cases (iv) and (v), the latest estimated channels were used.

The relative error was large when we did not predict the channel. This is because the channel changed largely during τ of 2.5 ms due to the motion of the UE and scatterers. The relative error of the linear extrapolation or AR-model-based channel prediction method was also large similarly to the case of "Non-Prediction". In the simulation scenario, the frame
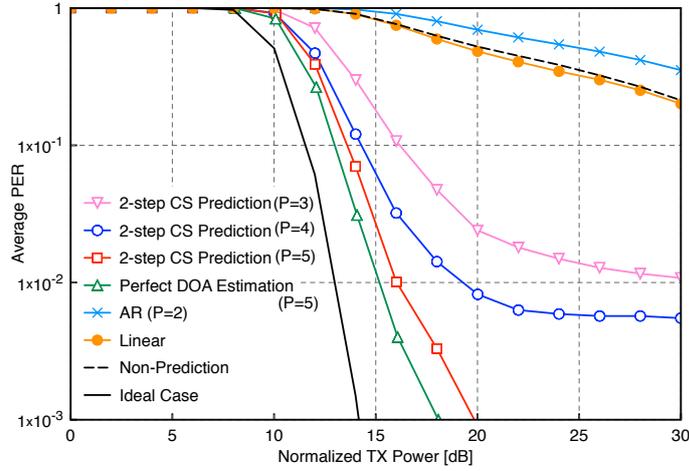
Figure 2.9: Average packet error rate for UE1 versus normalized TX power. Reprinted from [9] with permission (©2019 IEEE).

duration T_f was 5 ms, and the channels were observed every 5 ms. The correlation between adjacent observed channels was low in Jakes' environment due to $f_D T_f = 1$; therefore, the above conventional methods did not work well. Also, we assumed $f_D \tau = 0.5$. As stated in the Introduction, the prediction range for these methods is up to about 0.1 or 0.2. The $f_D \tau$ of 0.5 is beyond the applicable range. On the other hand, when using the proposed channel prediction method, the relative error was small. When the observation number P was 5, the performance of the proposed channel prediction was close to "Ideal Case".

Figure 2.9 plots the average packet error rates (PERs) for UE1 versus the normalized TX power, the same as in the above-mentioned cases. Note that we added the performance of the proposed channel prediction method for $P = 5$ on the assumption that the DOAs of the multipath components were perfectly known (Perfect DOA Estimation). In this case, the Doppler frequencies and complex amplitudes were obtained with the compressed sensing technique. Also in Fig. 2.9, we assumed that τ was 2.5 ms, which was the same as in Fig. 2.8.

The performance deteriorated when transmitting without channel prediction. The reason for this is as follows. Since the channels assumed for transmission at the BS have large errors, as shown in Fig. 2.8, the TX weights are not optimum, and the suppression effect of IUI and IStI deteriorates. The improvement in the linear extrapolation was small, and the performance of the AR-model-based channel prediction method was worse than that of the case without prediction. The reason for the deterioration is the same as that stated for Fig. 2.8.

On the other hand, when using the proposed channel prediction method, the PER performance greatly improved. The deterioration for the proposed channel prediction method
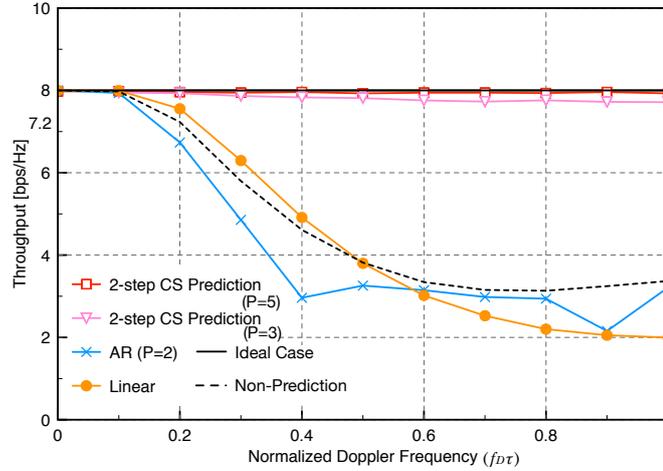
Figure 2.10: Throughput for UE1 versus normalized prediction range.
f_D was fixed at 200 Hz, and τ was changed from 0 to 5 ms. Reprinted from [9] with permission (©2019 IEEE).

$(P = 5)$ was less than 3 dB from "Ideal Case", and 1 dB from "Perfect DOA Estimation" at the PER of 10^{-2}. Also, the larger P, the better the PER. There are two reasons for this result. The first reason is that we can decorrelate the multipath components with MSSP by enlarging P. This can improve DOA estimation accuracy. The second reason is that we can estimate the Doppler frequencies and complex amplitudes with higher accuracy by increasing the dimension of the observation vector $\bar{\mathbf{v}}$ of MP of (2.27).

Figure 2.10 plots the throughput for UE1 versus the normalized Doppler frequency $(f_D\tau)$. The throughput is given by $8 \times (1 - \text{Average PER})$ bps/Hz because the data rate per user was 8 bits/symbol (8 bps/Hz) and error correction codes were not used. In this figure, the normalized TX power was 20 dB. Note that the throughput for "Ideal Case" was 8 bps/Hz, independent of $f_D\tau$. The f_D was fixed at 200 Hz, and τ was changed from 0 to 5 ms for determining $f_D\tau$. The throughputs for the conventional methods deteriorated when $f_D\tau$ was greater than 0.1. This is similar to "Non-Prediction". The reason for this is because we had $f_D T_f = 1$, as stated previously. The proposed channel prediction method, however, exhibited much better throughput performance. It can maintain a high throughput, even when τ is long.

2.7 Conclusion

We proposed an SOS channel prediction method using the 2-step compressed sensing technique. This method resolves an arrival signal to a UE into individual multipath components by estimating the DOAs with first-step compressed sensing. In the second step, we estimate

the Doppler frequencies and their complex amplitudes using the estimated DOA information. We applied the proposed method to a multi-user MIMO system. The method greatly improved the PER performance and throughput compared with the conventional methods. It should be noted that the proposed method does not require many pilot symbols. This feature is suitable, especially for massive MIMO systems.

We assumed stationary environments, viz., the DOA, the Doppler frequency, and complex amplitude of each multipath component do not change during the time interval of interest. In real mobile radio environments, however, these parameters are slowly time-variant. For future work, we will improve the proposed method in such a way that it can track the time-variant parameters. As for the DOA tracking, the technique proposed by Zhao et al. [50] may be used for the channel prediction.

In this paper, we have proposed downlink channel prediction using the DOAs and complex amplitudes of multipath components estimated at UE. This technique can be applied to frequency division duplex systems. For time division duplex systems, we can predict downlink channels using those values estimated at a BS because of channel reciprocity. We can place many antennas at a BS and realize a massive MIMO system. In this case apart from compressed sensing, we can apply other techniques to DOA estimation such as deep learning [51], which is an emerging technology. Also, it is possible to estimate both the azimuth and elevation angles using a full-dimension MIMO system [52], which is expected to resolve an arrival signal into multipath components more accurately.

Chapter 3

Co-channel Interference Suppression for DSTBC transmission

In this chapter, the author examines CCI supression scheme for DSTBC transmission.

3.1 Introduction

In wireless communications, diversity techniques using multiple antennas can be used to suppress multipath fading. In particular, STBC (Space-Time Block Coding) or DSTBC (Differential Space-Time Block Coding) are used in various wireless communication systems because the received signal processing is very straightforward [53]– [56]. Similarly, a transmission diversity scheme where each mobile terminal receives signals from two or more base stations is expected to produce a link with higher reliability. This system is often called "macro-diversity" [57]. However, just transmitting the same signal from both base stations may cause the signals to cancel each other and instead produce severe fading under certain phase relationships between the two. In particular, this effect, known as beat interference, becomes greatest when the signals from both base stations are received at the same level. To overcome this problem, [58] and [60] show that beat interference can be reduced by adding different frequency or phase offsets at each base station antenna and using DSTBC for the transmission. In this paper, it is assumed that DSTBC and a macro-diversity scheme are applied in each cell as in [57]. In a frequency reuse-1 scheme in which all the resources are used in every cell, Co-Channel Interference (CCI) at the cell edge can become severe. Compared with single-antenna transmission, greater CCI is observed in DSTBC transmission using multiple antennas. To overcome this problem, studies of CCI suppression techniques for SFBC and STBC transmission have been conducted [61], [62]. However, CCI suppression, especially for CCI at high power, has not been studied for DSTBC transmission. In this paper, we propose a CCI suppression method suitable for
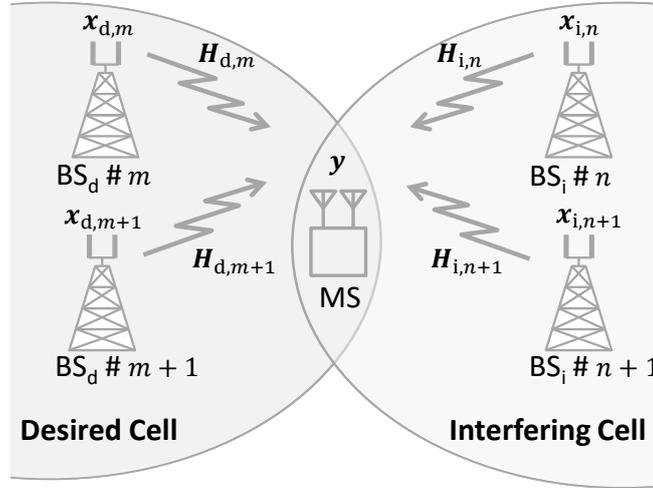
Figure 3.1: System model.

DSTBC transmission. Furthermore, we show how to apply the proposed CCI suppression method to a macro-diversity system. The results of our simulations show that the interference can be suppressed even when the number of arriving interference waves is more than twice the number of receiving antennas. The composition of this paper is as follows. Section 3.2 shows the system model assumed for this paper. Section 3.3 presents the proposed CCI suppression method, and how to apply the proposed method to a macro-diversity system. Section 3.4 show the setup and the results of the computer simulation. Finally, the conclusions are presented in Section 3.5.

3.2 System model

This paper assumes the system model shown in Fig. 3.1. Each transmitting base station forming a cell is equipped with $N_{\mathrm{tx}} = 2$ antennas, and the receiving mobile station (MS) is also equipped with $N_{\mathrm{rx}} = 2$ antennas. It is assumed that the system is operated in a frequency reuse-1 scheme, where each cell uses a common frequency resource. $M(M \geq 1)$ and $N(N \geq 1)$ denote the number of desired BSs (BSd) and interfering BSs (BSi), respectively. The RX signal vector $\boldsymbol{y}(t) = [y_0(t), y_1(t)]^{\mathrm{T}}$ at the MS with 2 RX antennas is written as

$$\boldsymbol{y}(t) = \sum_{m=0}^{M-1} \boldsymbol{H}_{\mathrm{d},m}(t)\boldsymbol{x}_{\mathrm{d},m}(t) + \sum_{n=0}^{N-1} \boldsymbol{H}_{\mathrm{i},n}(t)\boldsymbol{x}_{\mathrm{i},n}(t) \tag{3.1}$$

where $\boldsymbol{x}_{\mathrm{d},m}(t) = [x_{\mathrm{d}m,0}(t), x_{\mathrm{d}m,1}(t)]^{\mathrm{T}}$ denotes the TX signal vector from the mth BSd ($m = 0, 1, ..., M-1$), $\boldsymbol{x}_{\mathrm{i},n}(t) = [x_{\mathrm{i}n,0}(t), x_{\mathrm{i}n,1}(t)]^{\mathrm{T}}$ denotes the TX signal vector from the

nth BSi ($n = 0, 1, ..., N − 1$), $h_{\mathrm{d}m,pq}$ denotes the parameters of the channel between #m BSd and the RX antennas at the MS, $h_{\mathrm{i}n,pq}$ denotes the parameters of the channel between #n BSi and the RX antennas at the MS($p = 0, 1, ..., N_{\mathrm{rx}} − 1, q = 0, 1, ..., N_{\mathrm{tx}} − 1$), $\boldsymbol{H}_{\mathrm{d},m}(t)$ and $\boldsymbol{H}_{\mathrm{i},n}(t)$ denote the channel matrices which are formed from $h_{\mathrm{d}m,pq}$ and $h_{\mathrm{i}n,pq}$, respectively. Here, the thermal noise term which would usually be added to the RX signal is omitted for simplicity.

In the following, we first consider a case where there is one BSd and one BSi. In this case, Equation (3.1) can be rewritten as follows:

$$
\begin{bmatrix} y_0(t) \\ y_1(t) \end{bmatrix} = \begin{bmatrix} h_{\mathrm{d},00}(t) & h_{\mathrm{d},01}(t) & h_{\mathrm{i},00}(t) & h_{\mathrm{i},01}(t) \\ h_{\mathrm{d},10}(t) & h_{\mathrm{d},11}(t) & h_{\mathrm{i},10}(t) & h_{\mathrm{i},11}(t) \end{bmatrix} \begin{bmatrix} x_{\mathrm{d},0}(t) \\ x_{\mathrm{d},1}(t) \\ x_{\mathrm{i},0}(t) \\ x_{\mathrm{i},1}(t) \end{bmatrix} \tag{3.2}
$$

Here, the BS numbers m, n are omitted for simplicity. In Equation (3.2), since the number of arriving waves is greater than the number of receiving antennas, the receiver cannot distinguish all the arriving signals, which is also called an under-determined problem. To overcome this under-determined problem, the proposed method increases the dimensionality of the RX signal vector $y(t)$ by expanding the channel matrix based on the DSTBC coding rule. This rewrites Equation (3.2) into a determined form and suppresses the interference even when the number of incoming interfering waves is more than twice the number of receiving antennas. Note that, in order to distinguish between BSd and BSi, this paper assumes that the receiver can discern the channel matrix using the orthogonal pilot included in the radio frame. The orthogonal pilot is a signal used to distinguish the desired cell from the interfering cell.

3.3 CCI suppression method for DSTBC transmissiona

3.3.1 Expanding the channel matrix based on the DSTBC coding rule

In this subsection, we describe the basic principles of a scheme that can suppress numbers of interfering signals beyond the antenna degrees of freedom by expanding the channel matrix based on the DSTBC coding rules and performing interference suppression as a determined problem. First, the modulation and demodulation principles of DSTBC transmission using two antennas are presented. In DSTBC modulation, the subject of this paper, STBC is applied to two transmit symbols and the modulated signal is generated by taking the difference of the STBC blocks [54]. This process allows the receiver to achieve diversity by a simple process of differential processing between the STBC blocks. When the transmitter sends 2 symbols $s_k(t), s_k(t + 1)$ in two symbol periods, which lies within a single STBC block, the ith DSTBC block $p(p \geq 1)$ (a 2×2 matrix) is represented by the following equation.

$$
\begin{bmatrix} c_0(p) & c_1(p) \\ -c_1^*(p) & c_0^*(p) \end{bmatrix} = \begin{bmatrix} c_0(p-1) & c_1(p-1) \\ -c_1^*(p-1) & c_0^*(p-1) \end{bmatrix} \begin{bmatrix} s_k(p) & -s_{k+1}^*(p) \\ s_{k+1}(p) & s_k^*(p) \end{bmatrix} \tag{3.3}
$$

Here, $c_0(0)$ and $c_1(0)$ are the initial values for differential coding. In the DSTBC block matrix on the left-hand side of Equation (3.3), the column direction corresponds to the transmit antenna and the row direction corresponds to the symbol period.

At the receiver side, the received signals $y(t)$ and $y(t+1)$ of the two symbol periods can be transformed as follows, and the difference processing between the blocks can be used to obtain the estimated symbol values s_k and s_{k+1}.

$$\begin{bmatrix} \hat{s}_k & \hat{s}_{k+1} \end{bmatrix} = \begin{bmatrix} y(t) & -y^*(t+1) \end{bmatrix} \begin{bmatrix} y(t-2) & -y^*(t-1) \\ y(t-1) & y^*(t-2) \end{bmatrix}^{\mathrm{H}} \tag{3.4}$$

Next, it is explained how to expand the channel matrix based on the DSTBC coding rule. In Equation (3.2), the received signals at two symbol periods t and $t+1$ can be expressed as a matrix as follows:

$$\begin{bmatrix} y_0(t) & y_0(t+1) \\ y_1(t) & y_1(t+1) \end{bmatrix} = \begin{bmatrix} h_{\mathrm{d},00}(t) & h_{\mathrm{d},01}(t) & h_{\mathrm{i},00}(t) & h_{\mathrm{i},01}(t) \\ h_{\mathrm{d},10}(t) & h_{\mathrm{d},11}(t) & h_{\mathrm{i},10}(t) & h_{\mathrm{i},11}(t) \end{bmatrix} \begin{bmatrix} x_{\mathrm{d},0}(t) x_{\mathrm{d},0}(t+1) \\ x_{\mathrm{d},1}(t) x_{\mathrm{d},1}(t+1) \\ x_{\mathrm{i},0}(t) \ x_{\mathrm{i},0}(t+1) \\ x_{\mathrm{i},1}(t) \ x_{\mathrm{i},1}(t+1) \end{bmatrix} \tag{3.5}$$

Here we assume that there is negligible change in the channel conditions between t and $t+1$.

When the transmitted signal from each base station is DSTBC modulated at times t and $t+1$ as one STBC block, using the coding relationship in Equation (3.3), following equations are obtained.

$$x_{\mathrm{d},0}(t+1) = -x_{\mathrm{d},1}^*(t) \tag{3.6}$$

$$x_{\mathrm{d},1}(t+1) = x_{\mathrm{d},0}^*(t) \tag{3.7}$$

$$x_{\mathrm{i},0}(t+1) = -x_{\mathrm{i},1}^*(t) \tag{3.8}$$

$$x_{\mathrm{i},1}(t+1) = x_{\mathrm{i},0}^*(t) \tag{3.9}$$

In this case, the received signals at the two antennas for the two symbol periods are converted into a vector, and the four-dimensional received signal vector can be expressed as in Equation (3.10) based on the relationships formed by complex conjugation and sign inversion.

$$\begin{bmatrix} y_0(t) \\ -y_0^*(t+1) \\ y_1(t) \\ -y_1^*(t+1) \end{bmatrix} = \begin{bmatrix} h_{\mathrm{d},00} & h_{\mathrm{d},01} & h_{\mathrm{u},00} & h_{\mathrm{i},01} \\ -h_{\mathrm{d},01}^* & h_{\mathrm{d},00}^* & -h_{\mathrm{i},01}^* & h_{\mathrm{i},00}^* \\ h_{\mathrm{d},10} & h_{\mathrm{d},11} & h_{\mathrm{u},10} & h_{\mathrm{i},11} \\ -h_{\mathrm{d},11}^* & h_{\mathrm{d},10}^* & -h_{\mathrm{i},11}^* & h_{\mathrm{i},10}^* \end{bmatrix} \begin{bmatrix} x_{\mathrm{d},0}(t) \\ x_{\mathrm{d},1}(t) \\ x_{\mathrm{i},0}(t) \\ x_{\mathrm{i},1}(t) \end{bmatrix} \tag{3.10}$$

The above equation is a determined problem for estimating the four-dimensional transmit signal vector from the four-dimensional receive signal vector, and each signal can be separated by applying MMSE (Minimum Mean Square Error) or other spatial filtering to the expanded channel matrix.

The next subsection describes how the weights are generated.

3.3.2 Interference suppression weight generation

The following subsection describes how to generate the weights to suppress interfering signals using the expanded channel matrix presented in the previous section. Here, the expanded channel matrices (4×2 matrix) of BSd and BSi are defined as $\boldsymbol{H}_\mathrm{d}$ and $\boldsymbol{H}_\mathrm{i}$, respectively:

$$\boldsymbol{H}_\mathrm{d} = \begin{bmatrix} h_\mathrm{d,00} & h_\mathrm{d,01} \\ -h_\mathrm{d,01}^* & h_\mathrm{d,00}^* \\ h_\mathrm{d,10} & h_\mathrm{d,11} \\ -h_\mathrm{d,11}^* & h_\mathrm{d,10}^* \end{bmatrix} \tag{3.11}$$

$$\boldsymbol{H}_\mathrm{i} = \begin{bmatrix} h_\mathrm{i,00} & h_\mathrm{i,01} \\ -h_\mathrm{i,01}^* & h_\mathrm{i,00}^* \\ h_\mathrm{i,10} & h_\mathrm{i,11} \\ -h_\mathrm{i,11}^* & h_\mathrm{i,10}^* \end{bmatrix} \tag{3.12}$$

The 2×4 matrix MMSE weights $\boldsymbol{W}_\mathrm{mmse}$ for estimating the desired transmit signal vector to be received via the channel matrix $\boldsymbol{H}_\mathrm{d}$ are expressed in Equation (3.13), where σ is the thermal noise term and $\boldsymbol{I}_{44}$ is the 4×4 identity matrix.

$$\boldsymbol{W}_\mathrm{mmse} = \boldsymbol{H}_\mathrm{d}^\mathrm{H}(\boldsymbol{H}_\mathrm{d}\boldsymbol{H}_\mathrm{d}^\mathrm{H} + \boldsymbol{H}_\mathrm{i}\boldsymbol{H}_\mathrm{i}^\mathrm{H} + \sigma\boldsymbol{I}_{44})^{-1} \tag{3.13}$$

This is similar to the CCI suppression weights for SFBC and STBC described in [61] and [62].

3.3.3 Application to macro-diversity system

Since the previous sections have dealt with the cases $M = 1$ and $N = 1$, where there is one desired station and one interfering station, respectively, the signals can be separated by increasing the dimensionality of the received signal vector from two to four by channel matrix expansion. Here, we show how to apply this method to the case where at least two desired or interfering stations are seen by the MS. In the following, we present the solutions for applying the CCI suppression scheme for DSTBC transmission described in the previous section to a macro-diversity system in which beat interference is reduced by the phase offset scheme presented in the literature [58], [59].

When the phase offset scheme is applied to a macro-diversity system, a transformation based on phase rotation is performed independently for each base station for the DSTBC transmission block. The principle is that signals arriving from different base stations in the same cell have the same data symbols but different waveforms at the receiver, thus reducing beat interference. On the other hand, since different waveforms arrive at the receiver, even if the received signal vector and channel matrix are expanded as in Equation (3.10), more signals will arrive than the dimensionality of the expanded received signal vector, again causing the under-determined problem. The solution to this problem is as follows.

Table 3.1: Simulation parameters.

Number of BSd (M)	1, 2
Number of BSi (N)	1, 2
Number of antennas for BS and MS	2
Assumed system	Macro-diversity in each cell
	and Frequency reuse-1 scheme in every cell.
Beat interference suppression	Phase offset scheme [58], [59]
SIR	0 - 20dB
Channel	1-path Rayleigh fading
Modulation	DSTBC + QPSK
Block / Symbol synchronization.	Ideal

The phase rotations of each base station in the phase offset scheme can be viewed as a matrix transformation based on the phase rotator matrix $\boldsymbol{D}$ applied to the transmission vector. Then, the following equation holds:

$$\boldsymbol{y}(t) = \sum_{m=0}^{M-1} \boldsymbol{H}_{\mathrm{d},m}(t)\boldsymbol{D}_{\mathrm{d},m}\boldsymbol{x}_{\mathrm{d},0}(t) + \sum_{n=0}^{N-1} \boldsymbol{H}_{\mathrm{i},n}(t)\boldsymbol{D}_{\mathrm{i},n}\boldsymbol{x}_{\mathrm{i},0}(t) \tag{3.14}$$

Here, the equivalent channels are defined as follows:

$$\bar{\boldsymbol{H}}_{\mathrm{d}}(t) = \sum_{m=0}^{M-1} \boldsymbol{H}_{\mathrm{d},m}(t)\boldsymbol{D}_{\mathrm{d},m} \tag{3.15}$$

$$\bar{\boldsymbol{H}}_{\mathrm{i}}(t) = \sum_{n=0}^{N-1} \boldsymbol{H}_{\mathrm{i},n}(t)\boldsymbol{D}_{\mathrm{i},n} \tag{3.16}$$

where $\boldsymbol{D}_{\mathrm{d},m}$ denotes the phase rotator matrix for the mth BSd, and $\boldsymbol{D}_{\mathrm{i},n}$ denotes the phase rotator matrix for the nth BSi. By performing the matrix expansion based on Equation (3.10) using these equivalent channel matrices, Equation (3.14) is transformed into a determined problem. This means that the desired signal can be separated from the interfering signals even in a macro-diversity system using the phase-offset scheme.

3.4 Simulation

3.4.1 Simulation setup

The Bit Error Rate (BER) characteristics of the proposed scheme under CCI conditions are evaluated by computer simulation. The following three evaluation targets are compared,
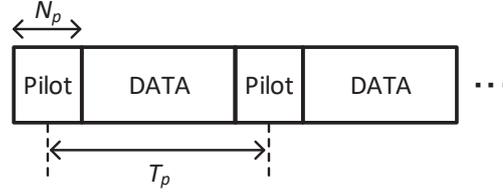
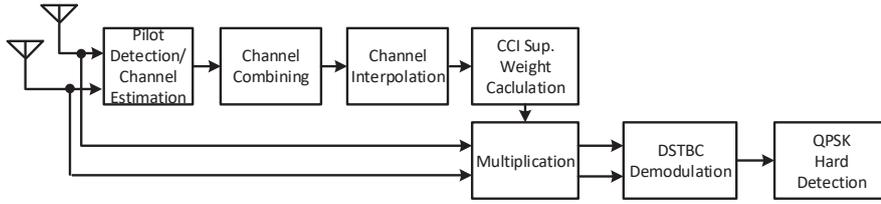Figure 3.2: Frame format. Reprinted from [10] with permission (©2022 IEICE).

Figure 3.3: Block diagram of proposed receiver. Reprinted from [10] with permission (©2022 IEICE).

and the signal-to-noise ratio (SNR) and signal-to-interference ratio (SIR) are varied to evaluate the BER.
(1) DSTBC demodulation is performed without applying any interference suppression (w/o CCI sup.)
(2) MMSE-IRC, which is considered for LTE-Advanced in [62], is applied as a technique to suppress CCI without channel expansion processing (CCI sup. (w/o ch. exp.))
(3) The proposed channel expansion is performed for both the desired and interfering channels and W_{mmse} in Equation (3.13) is applied (CCI sup. (mmse)).

Table 3.1 shows the simulation parameters. In this simulation, the modulation scheme is DSTBC + QPSK. The number of desired base stations BSd (M) is 1 or 2, and the number of interfering base stations BSi (N) is also 1 or 2. Each BS and MS has 2 antennas. Since the proposed CCI suppression method requires channel information, it is configured as shown in Fig. 3.2, where the pilot signal is periodically inserted among the data symbols. As a simple measure against the orthogonality of the weights being broken due to the varying propagation time of each channel, first-order interpolation of the channel parameters is performed between the pilot signals, and the weights are recalculated with the interpolated channel parameters for each DSTBC block. The channel parameters for each BS antenna are estimated using the orthogonal pilot signals (insertion period T_p) with $N_p = 8$ [symbols]. In this evaluation, channel coding was omitted to confirm the basic performance of the interference suppression of the proposed method.

Fig. 3.3 shows the proposed receiver block configuration. First, the channel estimation is performed using the pilot signals included in the received signal. Channel combining

is performed using the channel transformation matrices in Equations (3.15) and (3.16). First-order interpolation is performed between the channel parameters estimated from the pilot signals. The CCI suppression weights are generated using the first-order interpolated channel estimate. The weights are multiplied by the received signal to perform interference suppression. The evaluation assumes that the symbol synchronization and block synchronization are ideal. Reference [63] proposes a synchronization scheme for DSTBC that achieves symbol synchronization and block synchronization simultaneously, and such a technique may be used for actual operations.

3.4.2 Simulation result

Fig. 3.4 shows the SNR vs. BER characteristics for each weight at SIR = 0 dB. First, the channel is assumed to have quasi-static Rayleigh fading so that it is not affected by interpolation errors or channel combining availability. The BSd and the BSi observed at the receiver are for one station each ($M = 1, N = 1$). In this setup, two signals from the BSd and two signals from the BSi arrive at the MS, for a total of four signals. Without interference suppression (w/o CCI Sup.), the characteristics are significantly degraded due to the very high interference power. The MMSE-IRC without channel matrix expansion (CCI-Sup. (w/o ch. exp.)) also has a large error rate. This is due to the fact that it is not possible to generate complete nulls, since two interfering signals are arriving for two antenna degrees of freedom. On the other hand, when the proposed channel matrix expansion is performed (CCI Sup. (mmse)), the error rate is greatly improved.

Fig. 3.5 shows the SNR vs. BER characteristics (SIR = 0 dB) with and without channel combining per Equations (3.14) – (3.16). Let us assume that the BSd and the BSi observed by the receiver are for two stations ($M = 2, N = 2$), respectively. For each weight with channel matrix expansion, the results are shown when the channel matrices are combined according to Equations (3.15) and (3.16) (w/ch. comb.) and when they are not combined (w/o ch. comb.). In this setup, the two antennas receive four signals from each BSd and BSi, for a total of eight signals. The results show that without channel combining, sufficient interference suppression cannot be achieved. This is due to the under-determined problem. On the other hand, the interference suppression works well when the channel combining process is applied. This is because it is a decision problem.

Fig. 3.6 shows the SIR vs. BER characteristics for each weight at SNR = 20 dB. Let us assume that the BSd and the BSi observed by the receiver are for two stations ($M = 2, N = 2$), respectively. It can be seen that each characteristic increases asymptotically as the SIR increases, and diversity alone is sufficient in the large SIR region. The results show that the proposed method is effective in environments with stronger interference than 20 dB SIR.

Fig. 3.7 shows the SIR versus BER characteristics for each weight in a time-varying Rayleigh fading environment ($M = 2, N = 2$, SNR = 20 dB). Here, the symbol rate-normalized maximum Doppler frequency $f_D T_s$ is set to 0.5% based on the literature [63], and it is considered that the orthogonality of the weights is preserved to some extent by the first-order interpolation [27]. Since the channel interpolation is a simple first-order interpolation, an overall degradation can be seen in the low SIR region relative to Fig. 3.6.
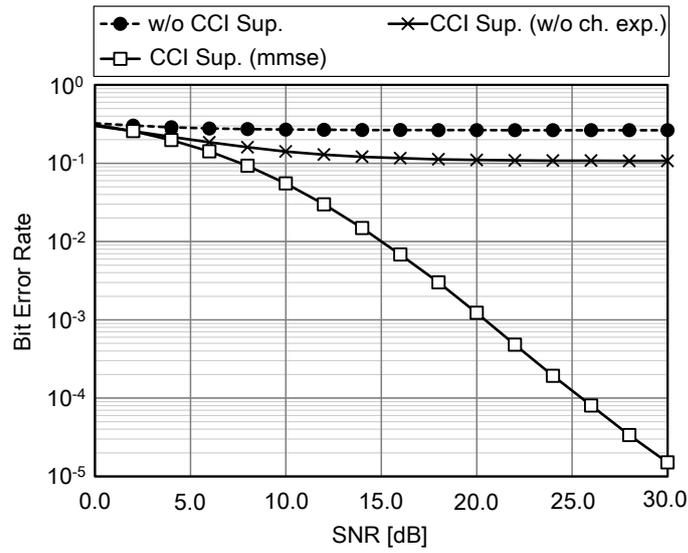
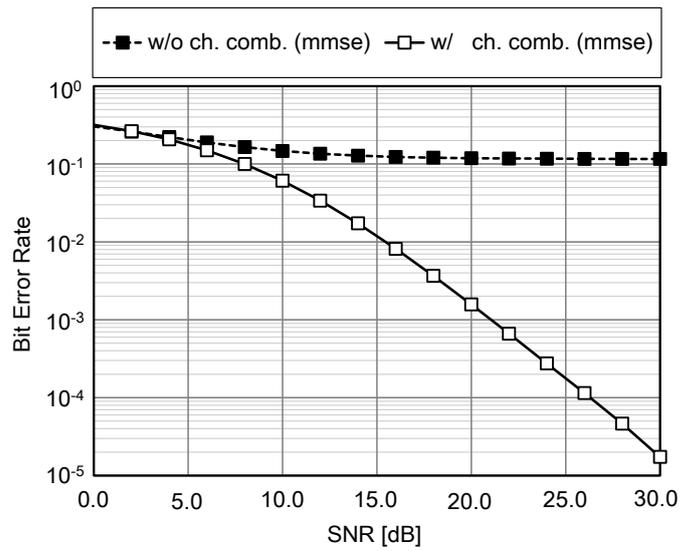Figure 3.4: SNR vs. BER for each CCI supression weight.

Figure 3.5: SNR vs. BER for channel combining on/off.

However, the improvement provided by the proposed method can be confirmed even in time-varying environments.
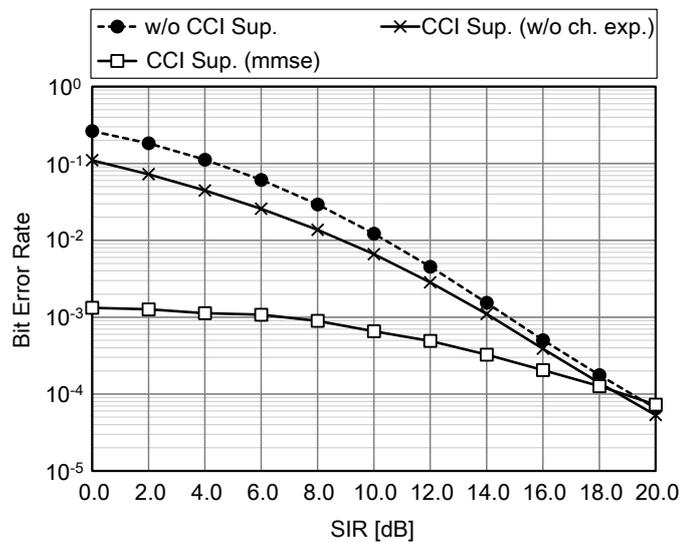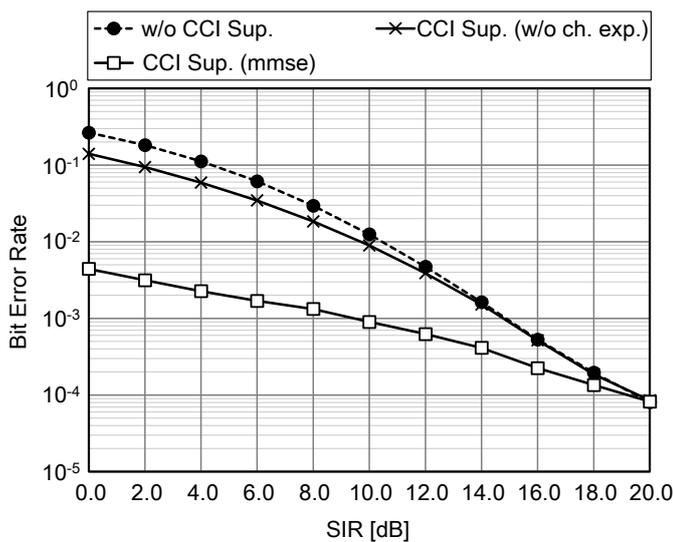
Figure 3.6: SIR vs. BER for each CCI supression weight.

Figure 3.7: SIR vs. BER for each CCI supression weight.

3.5   Conclusions

In this paper, we propose a CCI suppression method for DSTBC transmission. The results of our simulations show that the interference can be suppressed even when the number of arriving interference waves is more than twice the number of receiving antennas.

Chapter 4

An Adaptive Nonlinear Equalizer Utilizing Memory Polynomial for Wideband Satellite Communications

In this chapter, the author proposes an adaptive nonlinear equalizer utilizing memory polynomial for wideband satellite communications.

4.1   Introduction

In order to cope with the need for high speed, high capacity satellite communications, greater signal bandwidth and multi-level modulation are expected to be adopted. In wideband transmission, the receiver performance deteriorates due to nonlinear distortion in the amplifiers and linear distortion caused by group delay in the bandpass filters. In particular, multi-level modulation and a low roll-off factor lead to increased PAPR (Peak to Average Power Ratio), and this has a large effect on the nonlinear distortion of the transmitted signals. For example, 32APSK (Amplitude and Phase Shift Keying) transmission is adopted for DVB-S2 (Digital Video Broadcasting – Satellite Second Generation) [64], and 64APSK and higher transmission with 5% roll-off factor are adopted for DVB-S2X [65]. As a means of compensating for non-linear distortion, DPD (Digital Pre-Distortion) at the transmitter side is generally adopted. This method compensates the distortion by using the inverse of the characteristics of the nonlinear amplifiers. However, if the transmitter has insufficient circuit resources for this to be implemented, and if the linear distortion in the receiver also needs to be compensated for demodulation, it is useful to compensate both sources together at the receiver. The conventional approach to equalization at the receiver is adaptive linear equalization utilizing a linear FIR (Finite Impulse Response) filter [65], but this has difficulty compensating nonlinear distortion. Therefore, nonlinear equalization

methods based on nonlinear polynomial filters (e.g. Volterra filters) [66] [67] or neural networks [68] [69] have been proposed. These methods are effective for nonlinear compensation, but they do have some issues. The computational complexity of the neural network method is very high, and it needs advance training of the coefficients to enable it to adapt to the target system. In time-varying environments in which there are frequency or clock variations, Volterra equalization, which can adaptively update the coefficients, is more practical. However, there are two main issues with Volterra equalization. The first is similarly high computational complexity because the Volterra equalizer requires the estimation of a large number of filter coefficients to compensate the distortion. The other is that it is difficult to estimate all of the filter coefficients in a communication system with a limited number of known pilot symbols such as DVB-S2(X).

In this paper, we discuss our proposed adaptive nonlinear equalization [70] [71] and the results of a computer simulation and an experimental evaluation based on a FPGA (Field Programmable Gate Array) used to implement the proposed method. Our proposed equalizer is based on a memory polynomial [72] which reduces the number of filter coefficients compared to a Volterra equalizer. Furthermore, the proposed method enables the receiver to operate correctly even when the number of filter coefficients is greater than the number of known pilot symbols. In this method, a linear equalization part using a conventional linear filter and a non-linear equalization part using a polynomial filter are arranged in parallel, and their outputs are combined to compensate the linear and nonlinear distortions together. The proposed method first estimates the coefficients of the linear compensation part with known pilot symbols as in the conventional methods, with the coefficients of the nonlinear compensation part set to 0. Then, it updates both the linear and nonlinear parts' coefficients using a decision-directed LMS (Least Mean Square) algorithm. As a result, all of the filter coefficients are estimated using the same number of known pilot symbols as a conventional linear equalizer. The composition of this paper is as follows. Section 4.2 shows the system model assumed in this paper. Section 4.3 presents the proposed nonlinear equalization method, and Sections 4.4 and 4.5 show the setup and the results of the computer simulation and experimental evaluation, respectively. Finally, the conclusions are presented in Section 4.6.

4.2   System model

In this section, the satellite communication system model assumed in this paper is described. Figure 4.1 shows the block diagram of the satellite communication system. The generic satellite transmitter model used for the simulation is composed of an input bandpass filter (IMUX), a power amplifier and an output bandpass filter (OMUX) [64], [65]. These cause nonlinear distortions with memory effects and linear distortion of the transmit signals. In this model, the received signal $y(t)$ is denoted as follows:

$$y(t) = \kappa_{\mathrm{o}} * \left\{ \zeta\big(\kappa_{\mathrm{i}} * s(t)\big) \right\} + n(t), \tag{4.1}$$
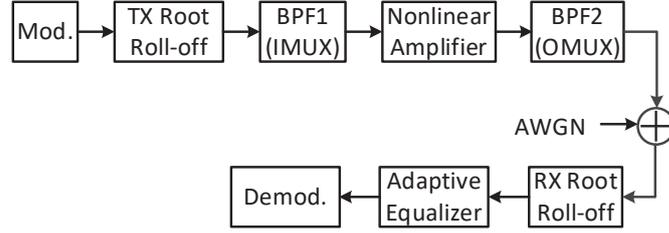
Figure 4.1: System model. Reprinted from [12] with permission (©2021 IEEE).

where $*$ is the convolution operator, κ_i and κ_o are the impulse responses of the IMUX filter and OMUX filter, $\zeta\{\cdot\}$ is the nonlinear function of the nonlinear amplifier, $s(t)$ is the output of the TX root roll-off filter and $n(t)$ is AWGN (Additive White Gaussian Noise). The above $y(t)$ represents the received signal with both nonlinear distortion and linear distortion with memory. In the next section, the proposed method which is able to compensate the above distortions at the receiver is described.

4.3 Adaptive Nonlineaer Equalizer

In this section, we discuss the proposed adaptive nonlinear equalizer based on a memory polynomial. First, nonlinear equalization utilizing a Volterra filter will be described. The kth output symbol of the Volterra equalizer $\tilde{x}_k$ is given by

$$\tilde{x}_k = \sum_{m_1=0}^{M-1} h_1(m_1)y(kP - m_1)+$$

$$\sum_{m_1=0}^{M-1} \sum_{m_2=0}^{M-1} \sum_{m_3=0}^{M-1} h_3(m_1, m_2, m_3)y(kP - m_1)y^*(kP - m_2)y(kP - m_3) + \cdots, \quad (4.2)$$

where $h_d(\cdot)(d = 1, 3, 5, ...)$ represents the filter coefficients, M denotes the depth of memory and P denotes the over sampling ratio. The number of Volterra equalizer coefficients for equation (4.2) is $\sum_{d=1,3,5,...}^{D} M^d$, meaning that the computational complexity is very high. Even if we select only $d = 1, 3$ as in equation (4.2), $M + M^3$ filter coefficients are required, and this is still large in terms of the hardware implementation. Therefore, we propose adaptive nonlinear equalization based on a memory polynomial which reduces the number of filter coefficients compared to the Volterra equalizer. To reduce the computational complexity, the proposed method only utilizes $m_1 = m_2 = m_3$ for equation (4.2), then the kth output symbol of the proposed equalizer $\tilde{x}_k$ is given by

$$\tilde{x}_k = \sum_{i=0}^{M-1} h_1(i)y(kP - i) + \sum_{i=0}^{M-1} h_3(i, i, i) |y(kP - i)|^2 y(kP - i). \quad (4.3)$$
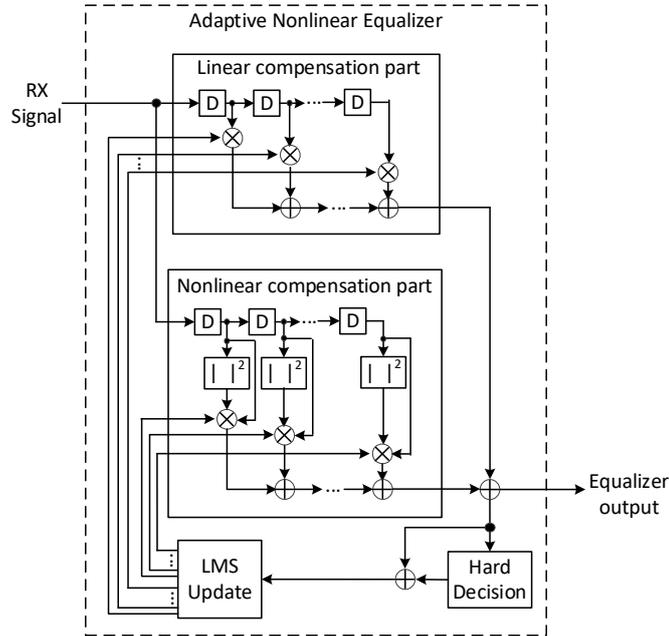
Figure 4.2: Block diagram of the proposed nonlinear equalizer. Reprinted from [9] with permission (©2019 IEEE).

The first term of equation (4.3) is the linear compensation part, which is equivalent to a conventional linear equalizer, and the second term of (4.3) is the 3rd order nonlinear compensation part. As in Fig. 4.2, the proposed method consists of two FIR filters in parallel whose inputs are $y(t)$ and $|y(t)|^2 y(t)$, respectively. As a result, the proposed method can reduce the number of filter coefficients from $M + M^3$ to $M + M$. Specifically, when $M = 14$, the proposed method can reduce the number of filter coefficients to about 1/100 in exchange for only 0.1 dB reduction of the satellite power efficiency [70]. Next, the filter coefficient estimation method to resolve the second issue with Volterra equalization introduced in Section 4.1 is described. The proposed method estimates the filter coefficients in the following two steps as in Fig. 4.3. First, this method estimates the coefficients of the linear compensation part by using the RLS (Recursive Least Square) algorithm [73] with known pilot symbols, while the coefficients of the nonlinear compensation part are set to 0. Then, it updates both the linear and nonlinear parts' coefficients using a decision-directed LMS algorithm. As a result, all of the filter coefficients are estimated using the same number of known pilot symbols as a conventional linear equalizer. The following details the process for estimating the coefficients of the linear compensation part using the RLS algorithm. The linear filter coefficients' vector $\boldsymbol{w} = [w_0, w_1, \cdots, w_{M-1}]^{\mathrm{T}}$ is calculated by the
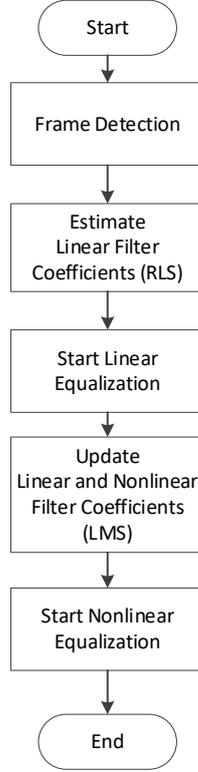
Figure 4.3: Flowchart of the filter coefficients estimation. Reprinted from [12] with permission (©2021 IEEE).

least squares method using the following equations:

$$\boldsymbol{Y}\boldsymbol{w} = \boldsymbol{x}, \tag{4.4}$$

$$\boldsymbol{w} = \left(\boldsymbol{Y}^{\mathrm{H}}\boldsymbol{Y}\right)^{-1}\boldsymbol{Y}^{\mathrm{H}}\boldsymbol{x}, \tag{4.5}$$

$$\boldsymbol{Y} = [\boldsymbol{y}^{\mathrm{T}}(k), \boldsymbol{y}^{\mathrm{T}}(k+1), \cdots, \boldsymbol{y}^{\mathrm{T}}(k+Q-1)]^{\mathrm{T}}, \tag{4.6}$$

$$\boldsymbol{y}(k) = [y(kP), y(kP+1), \cdots, y(kP+M-1)]^{\mathrm{T}}. \tag{4.7}$$

Here, we assume utilizing the $Q \times 1$ vector $\boldsymbol{x} = [x_k, x_{k+1}, \cdots, x_{k+Q-1}]^{\mathrm{T}}$ as the known pilot symbols in the SOF (Start of Frame) format defined in DVB-S2(X) for estimating the coefficients. Therefore, the size of the inverse matrix $(\boldsymbol{Y}^H\boldsymbol{Y})^{-1}$ for equation (4.5) is $M \times M$, which results in very high computational complexity. In contrast, our proposed method utilizes the RLS algorithm for lower complexity. Here, we define the correlation matrix $\boldsymbol{R} := \boldsymbol{Y}^H\boldsymbol{Y}$ and utilize a recurrence formula for calculating the inverse matrix as

follows:

$$\boldsymbol{R}^{-1}(i+1) = \boldsymbol{R}^{-1}(i) - \frac{\boldsymbol{R}^{-1}(i)\boldsymbol{y}^*(i)\boldsymbol{y}^{\mathrm{T}}(i)\boldsymbol{R}^{-1}(i)}{1+\boldsymbol{y}^{\mathrm{T}}(i)\boldsymbol{R}^{-1}(i)\boldsymbol{y}^*(i)}, \tag{4.8}$$

$$\boldsymbol{R}^{-1}(0) = \boldsymbol{I}. \tag{4.9}$$

Here, $\boldsymbol{R}(i)$ is the ith iteration matrix of $(i = 0, 1, \cdots, Q-1)$, and $\boldsymbol{I}$ is the $M \times M$ identity matrix. As a result, the linear filter coefficients' vector $\boldsymbol{w}$ can be estimated by equation (4.5). Then, we can update both the linear and nonlinear parts' coefficients using the decision-directed LMS algorithm. The kth input data sequence of the linear compensation part is $\boldsymbol{y}(k)$ as in (4.8), and that of the nonlinear compensation part is defined as

$$\boldsymbol{v}(k) = \begin{bmatrix} |y(kP)|^2 y(kP) \\ |y(kP+1)|^2 y(kP+1) \\ \vdots \\ |y(kP+M-1)|^2 y(kP+M-1) \end{bmatrix}. \tag{4.10}$$

The linear and nonlinear filter coefficients for the kth input data sequence are $\boldsymbol{w}(k)$ and $\boldsymbol{g}(k)$ respectively, so we can write the output of the proposed equalizer as:

$$\tilde{x}_k = \boldsymbol{w}^{\mathrm{T}}(k)\boldsymbol{y}(k) + \boldsymbol{g}^{\mathrm{T}}(k)\boldsymbol{v}(k). \tag{4.11}$$

In the LMS algorithm, the filter coefficients are updated for the reference signal $\hat{x}_k$ which is processed by the hard decoder using the following equations:

$$\boldsymbol{w}(k+1) = \boldsymbol{w}(k) + \mu_1 e(k)\boldsymbol{y}^*(k), \tag{4.12}$$

$$\boldsymbol{g}(k+1) = \boldsymbol{g}(k) + \mu_2 e(k)\boldsymbol{v}^*(k), \tag{4.13}$$

$$e(k) = \hat{x}_k - \tilde{x}_k. \tag{4.14}$$

Here, μ_1 and μ_2 are the step sizes for the linear and nonlinear parts respectively. As a result, all the filter coefficients are estimated from the same number of known pilot symbols as in a conventional linear equalizer. Also, our proposed equalizer is robust against clock timing offsets because it is a fractional space equalizer [65]. In the next section, the evaluation results show the performance improvement obtained with the proposed receiver.

4.4   Evaluation setup

Table 4.1 shows the parameters used in the experimental evaluation and the computer simulation. We assume 32APSK and 64APSK modulation with the mapping rule, frame format, IMUX and OMUX filter frequency characteristics (Figure 4.4) and nonlinear amplifier performance (Figure 4.5) introduced in [64] and [65]. The roll-off factor is 5% because the distortion effects of the nonlinear amplifier are large [74]. As shown in Section 4.3, our proposed method first estimates the filter coefficients using a 26 symbol SOF sequence

Table 4.1: **Evaluation parameters.**

Modulation	32APSK, 64APSK
Roll-off factor	5%
Depth of Memory (M)	14 (7 symbols)
Forward error correction	LDPC+BCH (code rate=5/6)
Oversampling ratio at RX	2
LMS stepsize(μ_1, μ_2)	1/512, 1/2048

with $\pi/2$ BPSK (Binary Phase Shift Keying) modulation by an RLS algorithm, which we update by an LMS algorithm using the coefficients estimated above. Figure 4.6 shows the overall configuration of the experimental evaluation. The experimental evaluations are performed according to the following steps. First, transmit waveforms (center frequency = 300MHz) with the linear and nonlinear distortion are generated using the TX signal digital generator (Fig. 4.7). Next, the digital transmit waveforms are converted to analog signals by the DAC (Digital to Analog Converter) and AWGN generated by the noise generator is added. After that, the baseband signals are input to the RX FPGA (Fig. 4.8) via the ADC (Analog to Digital Converter) and the DDC (Digital Down Converter). The RX FPGA compensates the signals with their linear and nonlinear distortions, and the frame error rate (FER) characteristics at each CNR (Carrier to Noise Ratio) are evaluated. In particular, the signal input to the RX FPGA is band-limited by the roll-off filter and adjusted to the desired level with DAGC (Digital Automatic Gain Control). The resampler adjusts the sampling rate of the input signals according to the clock deviation estimated by the frame detection unit. In the initial tap estimation circuit, the linear parts' coefficient estimation is performed using SOF. Also, the characteristics of the linear equalization method are shown as a conventional method, this characteristic being obtained by setting the nonlinear equalization filter coefficient to 0 in the same FPGA. For this evaluation, OBO is the measured power ratio in dB between the un-modulated carrier at saturation and the modulated carrier after OMUX [1], [75].

4.5 Result

Figures 4.9 - 4.12 show the equalizer output constellations of the conventional linear equalizer and the proposed equalizer when the OBO (Output Back-off)s are about 4.0 dB and 7.5 dB, respectively. When OBO = 7.5 dB, both constellations are similar because the nonlinear effect is small. On the other hand, when the nonlinear effect is large (OBO = 4.0 dB), the conventional linear equalizer cannot compensate the nonlinear distortion, while the nonlinear compensation effects of the proposed method can be seen. This shows that the proposed equalizer can represent the nonlinear distortion accurately.
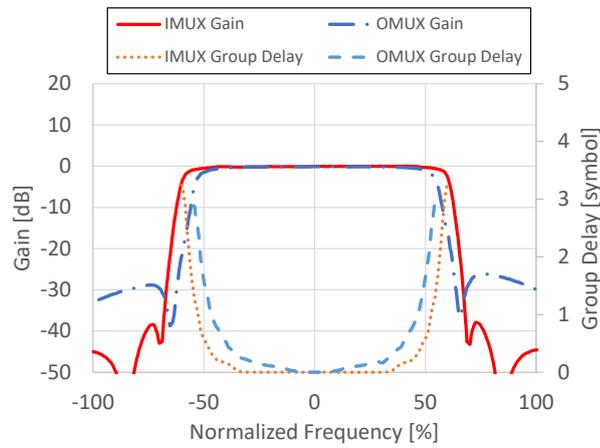
Figure 4.4: IMUX and OMUX filter parameters. Reprinted from [12] with permission (©2021 IEEE).
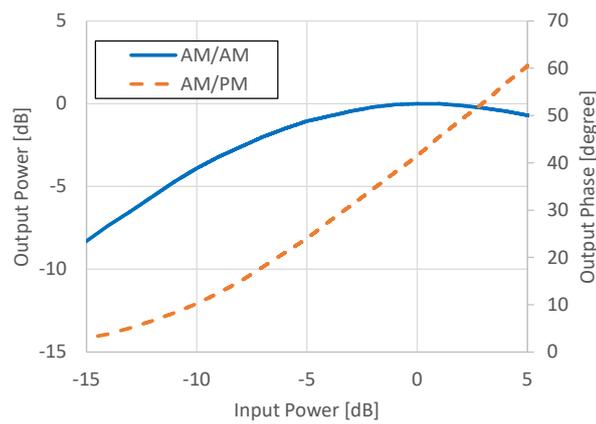

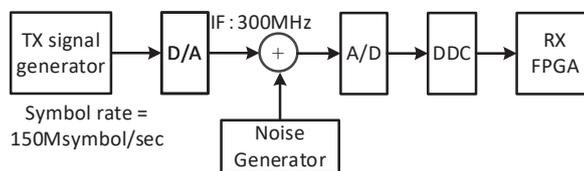Figure 4.5: Nonlinear amplifier parameters. Reprinted from [12] with permission (©2021 IEEE).

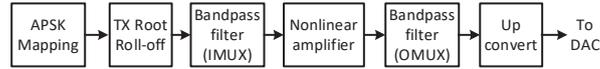Figure 4.6: Experimental system. Reprinted from [12] with permission (©2021 IEEE).

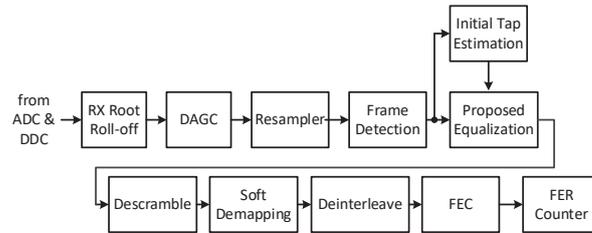Figure 4.7: Block diagram of TX Signal Generator. Reprinted from [12] with permission (ⓒ2021 IEEE).

Figure 4.8: Block diagram of RX FPGA. Reprinted from [12] with permission (ⓒ2021 IEEE).

Figure 4.13 shows the coded FER versus the CNR + OBO performance for 32APSK and 64APSK modulation, respectively. Improvement of CNR+OBO corresponds to improvement of the satellite power efficiency [75]. Here, we set the optimal OBO value for each method that is shown in Fig. 4.14. As shown in Fig. 4.13, the proposed method produces 1.3 dB improvement relative to the conventional linear equalizer ("Linear") at FER=10^{-4} for 32APSK transmission, and 1.7 dB improvement for 64APSK transmission. These results show that our method is more practical than other conventional methods. Figure 4.14 shows OBO versus $\triangle$ required CNR + OBO performance for 32APSK and 64APSK modulation, respectively. Large OBO reduces the nonlinear distortion. Thus, there exists an optimum operating point which well balances the output power and the nonlinear distortion. To quantify the overall effect, we resort to the concept of Total Degradation (TD) [74], defined as the sum in dB of the OBO and the increment in the CNR required to achieve a given FER=10^{-4} with respect to the case of a perfect linear amplifier as follows:

TD [dB] = $\triangle$Required CNR [dB] + OBO [dB].

Figure 4.14 shows the TD performance at different OBOs, and this denotes the optimum operating OBO that gives the lowest TD for each modulation. For 32APSK transmission, the optimum operating OBO is 4.8 dB ("Linear") and 3.9 dB ("Proposed"). For 64APSK transmission, the optimum operating OBO is 6.6 dB ("Linear") and 4.9 dB ("Proposed"). These results also show that the proposed method can improve the optimal OBO and the satellite power efficiency.

As an additional consideration, we discuss the reduction of the number of nonlinear filter coefficients for further performance improvement. Figure 4.15 shows examples of the amplitudes of each filter coefficient for the proposed method. Here, the modulation is 64APSK and OBO=4.0 dB. This figure proves that the amplitudes of the nonlinear parts'

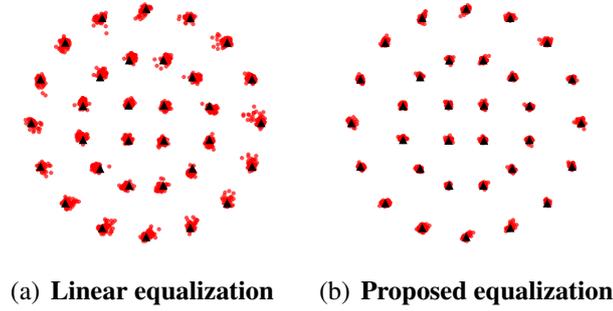(a) **Linear equalization**   (b) **Proposed equalization**

Figure 4.9: Equalizer output constellation for each method. （32APSK，TWTA, OBO=7.5 dB) Reprinted from [12] with permission (©2021 IEEE).

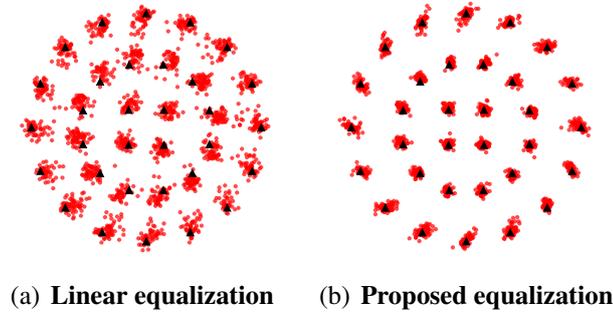(a) **Linear equalization**   (b) **Proposed equalization**

Figure 4.10: Equalizer output constellation for each method. （32APSK，TWTA, OBO=4.0 dB) Reprinted from [12] with permission (©2021 IEEE).

coefficients are smaller than those of the linear parts' coefficients, and that both ends of the nonlinear filter coefficients are almost 0. The proposed method consists of two FIR filters whose inputs are $y(t)$ and $|y(t)|^2 y(t)$, then the input signal power to the nonlinear filter is larger than that to the linear filter. As a result, it is considered that that the amplitudes of the nonlinear parts' coefficients are smaller. This point likely indicates that the number of nonlinear filter coefficients can be reduced, which we confirm by computer simulation. Figure 4.16 shows the coded FER performance changing the number of filter coefficients in the nonlinear parts. Note that this is not experimental performance but the results of a simulation. This is because varying the number of filter coefficients is difficult in a FPGA. However, the simulation result is almost the same as the experimental result, and the performance trends are maintained even in the experimental results. Here, we define the number of linear compensation parts' coefficients M_L, and the number of nonlinear compensation parts' coefficients M_{NL}. In the following evaluation, M_L is fixed at 14, and M_{NL} is changed to 2 ("1 symbol"), 6 ("3 symbol"), 10 ("5 symbol"), and 14 ("7
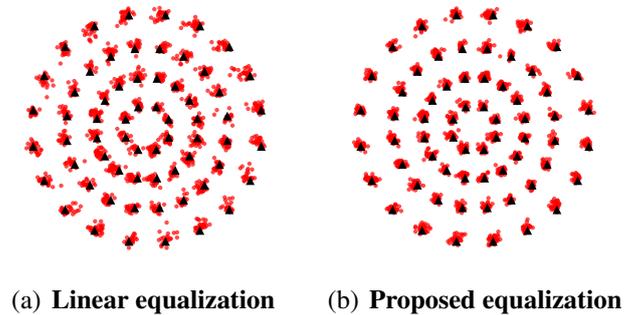
(a) **Linear equalization**   (b) **Proposed equalization**

Figure 4.11: Equalizer output constellation for each method. （64APSK, TWTA, OBO=7.5 dB) Reprinted from [12] with permission (©2021 IEEE).

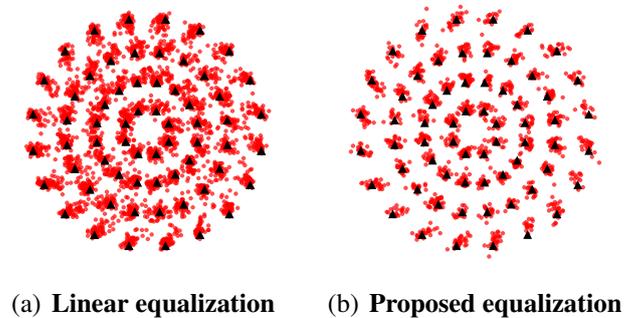(a) **Linear equalization**   (b) **Proposed equalization**

Figure 4.12: Equalizer output constellation for each method. （64APSK, TWTA, OBO=4.0 dB) Reprinted from [12] with permission (©2021 IEEE).

symbol"). The performance deteriorates when the number of nonlinear filter coefficients is "1 symbol" and "3 symbol". On the other hand, the FER performance of "5 symbol" and "7 symbol" are almost the same. From this result, in this environment, the proposed method can reduce the filter coefficients for up to 5 symbols, and this will also improve the convergence or tracking performance in the presence of frequency offsets or phase noise variation.

Figure 4.17 shows the performance when the roll-off factor is 20% and 5%. For each modulation and equalization method, the FER performance deteriorates when using a low roll-off factor. In particular, the performance degradation of "Linear (64, 5%)" is about 1.0 dB relative to a 5% roll-off factor. This is because combining multi-level modulation and a low roll-off factor leads to increased PAPR, and this has a large effect on the nonlinear distortion of the transmitted signals. On the other hand, the performance degradation of the proposed method is 0.1 - 0.2 dB relative to a low roll-off factor and this is smaller than with linear equalization. From this result, it is considered that the proposed method
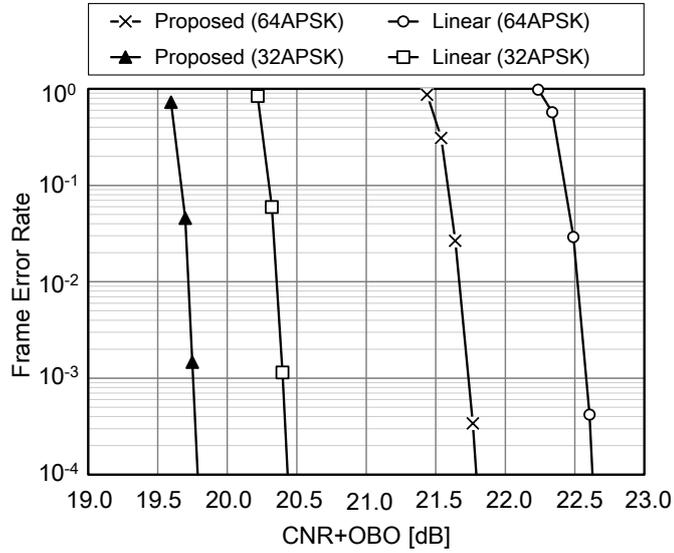
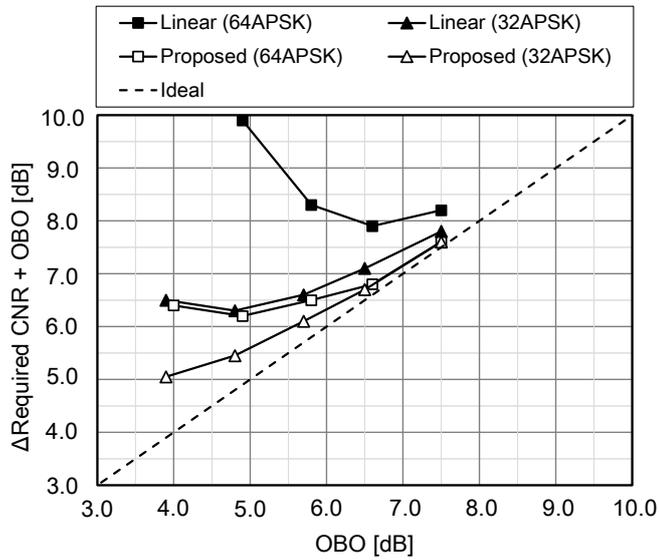Figure 4.13: Coded FER performance. Reprinted from [12] with permission (©2021 IEEE).

Figure 4.14: Total degradation performance for each method. Reprinted from [12] with permission (©2021 IEEE).

is robust against the large effect of nonlinear distortion due to the roll-off factor since this method can compensate the nonlinear distortion with high accuracy.
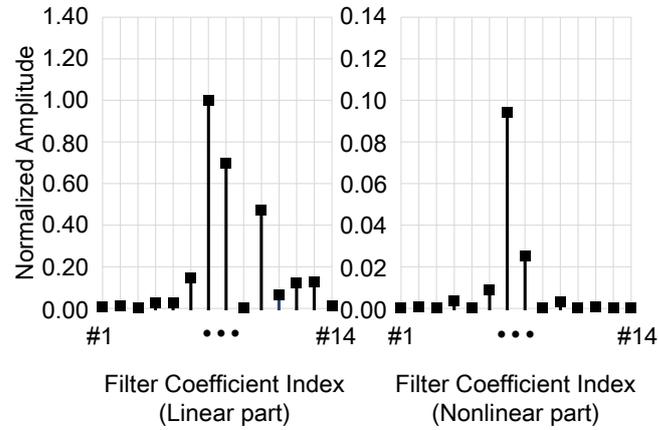
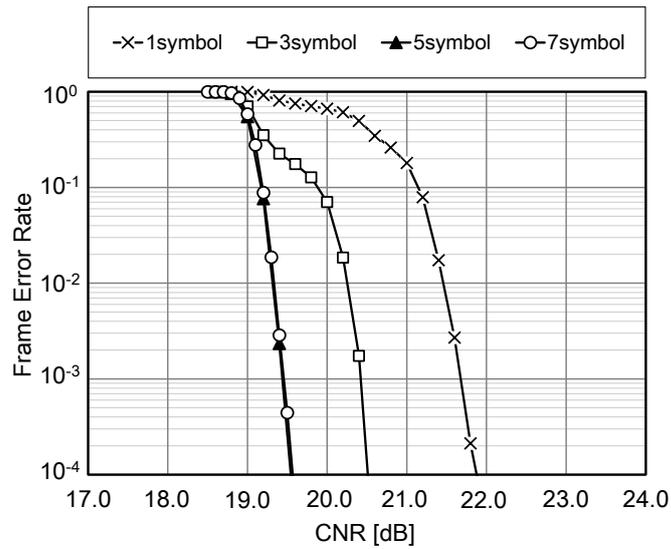Figure 4.15: Amplitudes of Each Filter coefficient. Reprinted from [12] with permission (©2021 IEEE).

Figure 4.16: Coded FER performance by changing the number of filter coefficients in the nonlinear parts. Reprinted from [12] with permission (©2021 IEEE).

4.6 Conclusions

This paper proposes an adaptive nonlinear equalizer based on a memory polynomial. The evaluation results show improved receiver performance for 32APSK and 64APSK transmission in the presence of both nonlinear and linear distortion. The proposed method
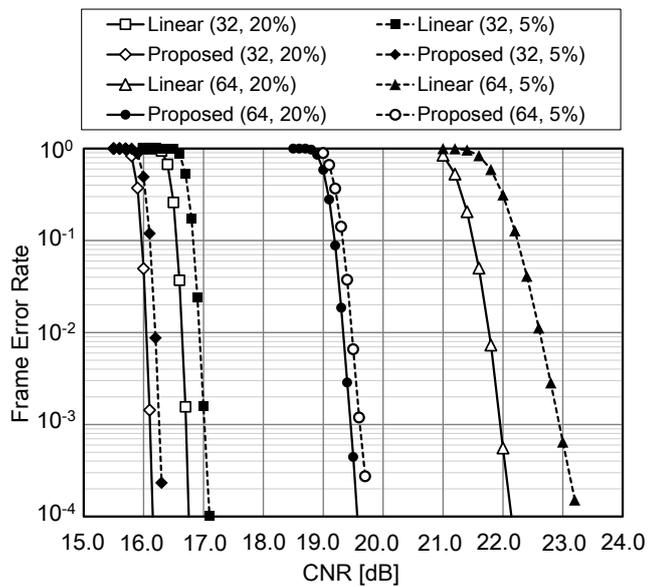
Figure 4.17: FER Performance for changing roll-off factor. Reprinted from [12] with permission (©2021 IEEE).

provides 1.3 dB (32APSK) and 1.7 dB (64APSK) improvement relative to a conventional linear equalizer. Moreover, this paper provides a method of reducing the number of nonlinear filter coefficients for further performance improvement and shows the effect of changing the roll-off factor in a satellite channel. These results verify the effectiveness of our proposed equalizer.

Chapter 5

Successive Interference Cancellation for Asynchronous Signal Collision in Space-based AIS

In this chapter, the author examines successive interference cancellation for asynchronous signal collision in space-based AIS.

5.1 Introduction

Automatic identification system (AIS) is a system in which a navigating vessel periodically transmits information such as the vessel's identification code, position, and speed to a shore station and the surrounding vessels [76]– [78]. The current terrestrial AIS has a limited communication distance with ships based on the elevation of the shore station and the frequency band, and can only obtain information on ships sailing in coastal areas (about 50 km from the shore station). For this reason, space-based AIS, which uses a satellite to capture the AIS signals, has come into use. Compared to terrestrial AIS, it is possible to track ships over a wide area, way beyond the coverage of any shore stations. In this system, however, the communication quality is degraded by interference between asynchronously colliding AIS signals from a large number of ships [79]– [81]. The signals have random relative delays, and are offset in frequency due to Doppler effects. Moreover, the number of signals arriving at the receiver is unknown, and sometimes the number of interfering waves arriving is more than the number of receiving antennas. Space-based AIS needs to overcome these problems.

Successive interference cancellation (SIC) is one technique for dealing with such a large number of signal collisions. SIC can suppress this interference by generating replicas of the interfering signals and subtracting the replicas from the desired signal. This makes it

possible to suppress interfering signals that exceed the number of antennas. When applying SIC to an AIS signal, the cancellation performance is degraded by the phase noise of each AIS transmitter [79], [81]. Further, since the filter bandwidth-time (BT) product for Gaussian minimum shift keying (GMSK) modulation is not specified for the AIS signals, the cancellation performance is also degraded when the replica is generated using a BT product different from that at the transmitter side.

In order to overcome these problems, this paper proposes a new SIC scheme that deals with asynchronous signal collisions.The proposed method successively estimates the delays and frequencies in order of signal strength, and then demodulates the signals. This enables us to generate replicas of the demodulated signals and to subtract the replicas from the desired signal in order to eliminate the interference caused by the signal collisions. In addition, this method generates especially accurate replicas by estimating the phase noise and filter BT product of each arriving signal, which would otherwise reduce the accuracy of the replicas, whence the interference cancellation performance can be improved. Moreover, combining the SIC with multi-antenna beamforming based on Chebyshev distribution can increase the number of signals which can be demodulated. In general, if the number of receiving signals is larger than the number of receiving antennas, it is difficult to detect the signals [82]. However, our proposed method can improve the packet error rate even when the number of interfering waves arriving is more than the number of receiving antennas.

The composition of this paper is as follows. Section 5.2 shows the system model assumed in this paper. Sections 5.3 and 5.4 present the proposed SIC for single and multiple antennas respectively, and Sections 5.5 present the setup and the results of the computer simulation. Finally, the conclusions are presented in Section 5.6.

5.2 System model for space-based AIS

In this section, the system model of the space-based AIS presented in this paper is described. Figure 5.1 shows the space-based AIS system. In this paper, it is assumed that the sattelite has a uniform linear array (ULA) with M antennas, and that each ship has one antenna for transmitting its AIS signal. The received signal $r_m(t)$ at the mth receive (RX) antenna is given by

$$r_m(t) = \sum_{k=0}^{K-1} a_k x_k(t - \tau_k) e^{j2\pi f_k t} e^{j\psi_{k,m}(t)} + n_m(t), \tag{5.1}$$

where K denotes the number of transmit signals from the ships, and $x_k(t)$ is the transmit signal of kth ship. Also, a_k, τ_k, and f_k denote the channel gain, delay, and frequency offset of the kth transmit signal, respectively. The last term $n_m(t)$ is the additive white Gaussian noise (AWGN) at the mth RX antenna. The phase variation $\psi_{k,m}(t)$ contains the phase rotation between the antennas, which depends on the dirrection of arrival (DOA) ϕ_k of the kth transmit signal, and the phase noise $\theta_k(t)$ due to using inexpensive oscillators in the

transmitters, as follows:

$$\psi_{k,m}(t) = \frac{2\pi d}{\lambda} m \sin \phi_k + \theta_k(t). \tag{5.2}$$

Here, d denotes the distance between the RX antennas and λ denotes the wavelength of the carrier. From the above, unknown parameters other than data $x_k(t)$ are a_k, τ_k, f_k, and $\psi_{k,m}(t)$.

5.3 SIC for asynchronous signal collisions using single RX antenna

This section first describes an SIC scheme that deals with asynchronous signal collisions for a single RX antenna ($M = 1$). Here, the subscript of $r_m(t)$ is abbreviated as $r(t)$ because $M = 1$. Figure 5.2 shows the block diagram of the proposed SIC method for a single RX antenna. The details are described in the following sections in the order of processing.

5.3.1 Delay & Frequency estimation

The proposed method estimates the delay and frequency offset of the strongest of the input signals within the aggregate received signal $r(t)$ using the known preamble symbols included in the AIS signals. Here, the oversampling ratio of $r(t)$ is Q.

First, the known preamble symbols $p_{f'}(t)$ with the frequency offset f' are prepared,

$$p_{f'}(t) = p(t)e^{j2\pi f't}. \tag{5.3}$$

Here, $p(t)$ is the set of known preamble symbols (the length is t_P symbols). Next, the method calculates the cross-correlation $y_{\tau',f'}$ between $r(t)$ and $p_{f'}(t)$ with varying delay τ':

$$y_{\tau',f'} = \sum_{t=\tau'}^{\tau'+t_P Q-1} r(t)p_{f'}^*(t - \tau'). \tag{5.4}$$

Then, the estimated delay $\hat{\tau}$ and the frequency offset $\hat{f}$ for the strongest signal are obtained by greedy searching of the combination (τ', f') that maximizes the power of $y_{\tau',f'}$,

$$(\hat{\tau}, \hat{f}) = \arg \max_{(\tau',f')} |y_{\tau',f'}|^2. \tag{5.5}$$

Here, the search ranges of (τ', f') are determined by the positional relation between the ships and the satellite.
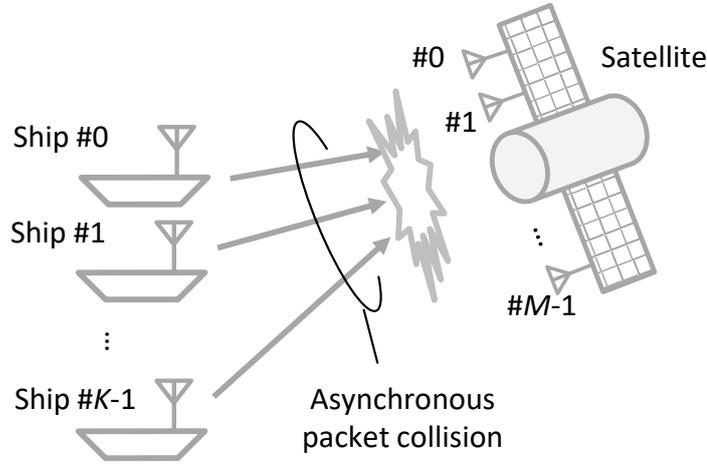
Figure 5.1: System model. Reprinted from [13] with permission (©2022 IEEE).
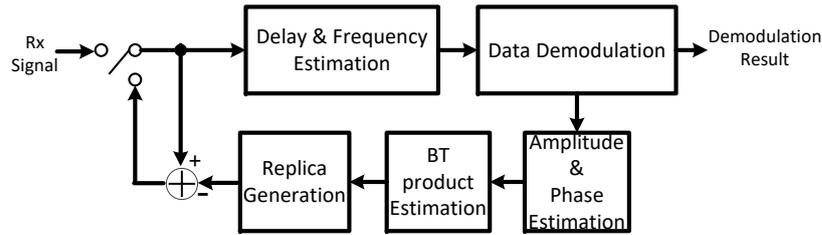

Figure 5.2: Block diagram of proposed SIC method for single RX antenna. Reprinted from [13] with permission (©2022 IEEE).

5.3.2 Demodulation

The proposed method demodulates the strongest transmit signal which is synchronized by $\hat{\tau}$ and $\hat{f}$. This signal is written as

$$\tilde{r}(t) = r(t + \hat{\tau})e^{-j2\pi\hat{f}t}, \tag{5.6}$$

and the demodulated bit sequences $\hat{x}(i)(i = 0, 1, ..., C - 1)$ are obtained by the GMSK demodulator whose input is $\bar{r}(t)(t = 0, Q, ..., Q(C - 1))$. Here, the GMSK demodulator has a phase tracking function which performs as in [83] and [84]. The phase tracking is needed for dealing with the phase noise and residual frequency offset. The input to the function is a GMSK signal which is down-sampled at the symbol timing, and the output is a set of demodulated bit sequences. Also, error detection is performed using the cyclic redundancy check (CRC) contained in the AIS signal. If an error is detected here, the subsequent canceling process is considered to fail, and the algorithm terminates. If no errors
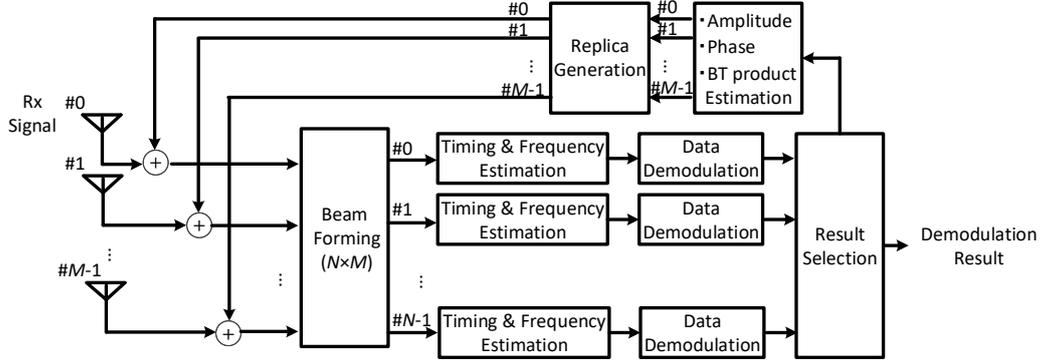
Figure 5.3: Block diagram for proposed SIC method with multiple antennas beamforming. Reprinted from [13] with permission (©2022 IEEE).

are detected, the various parameter (amplitude, phase variation, BT product) estimation and cancellation processes are performed.

5.3.3 Phase variation & amplitude estimation

The phase tracking described in the previous section may be sufficient for demodulation, but it is not accurate enough for the cancellation process. Therefore, phase variation estimation is performed for replica generation. The amplitude is also estimated. The estimated amplitude is a constant value because GMSK signals have a constant envelope. First, an oversampled (the ratio is Q) replica signal $z(t)$ is generated by re-modulating the bit sequences $\hat{x}(i)$ obtained in the demodulation process. The estimated phase variation $\hat{\psi}(t)$ and the estimated amplitude $\hat{a}$ are calculated as follows:

$$\hat{\psi}(t) = \arg\left[\tilde{r}(t)z^*(t)\right], \tag{5.7}$$

$$\hat{a} = \frac{1}{QC}\left|\sum_{t=0}^{QC-1}\frac{\tilde{r}(t)}{z(t)}\right|. \tag{5.8}$$

Here, $\hat{\psi}(t)$ may be estimated after applying a moving average filter to $\tilde{r}(t)z^*(t)$ in order to reduce any momentary variations.

5.3.4 BT product estimation

Since the filter BT product for GMSK modulation is not specified for the AIS signals, the cancellation performance is also degraded when the replica is generated with a BT product different from that used at the transmitter. Therefore, the proposed method estimates the BT product as described in this subsection. In the following explanation, the replica signal

generated by a GMSK modulator with the BT product b' is expressed as $z^{(b')}(t)$. The estimated BT product is obtained by subtracting the replica from the received signal while changing the BT product per the following equation:

$$\hat{b} = \arg\min_{b'} |r(t) - \hat{a}z^{(b')}(t - \hat{\tau})\mathrm{e}^{j2\pi\hat{f}t}\mathrm{e}^{j\hat{\psi}(t)}|^2. \tag{5.9}$$

Since the candidate value b' has only a few patterns at most, computational complexity is not a problem, and the BT product can be suitably estimated by this process.

5.3.5 Canceling

Using the processing described so far, all the estimated parameters for running the SIC can be obtained. Therefore, it is possible to remove the strongest interfering signal from the received signal $r(t)$,

$$\bar{r}(t) = r(t) - \hat{a}z^{(\hat{b})}(t - \hat{\tau})\mathrm{e}^{j2\pi\hat{f}t}\mathrm{e}^{j\hat{\psi}(t)}. \tag{5.10}$$

Then, the residual signal $\bar{r}(t)$ is input to "Delay & Frequency estimation". By repeating the above process, each transmit signal can be separated and demodulated even in an environment where multiple waves are interfering.

5.4 Expansion to multiple antennas

This section describes how to extend SIC for asynchronous signal collisions using a single RX antenna to multiple RX antennas. Figure 5.3 shows the block diagram of the proposed SIC method with multi-antenna beamforming. In a single-antenna SIC, if the power difference between the asynchronously colliding signals is small, the effects of the interference can make demodulation difficult, and this can make proper interference cancellation difficult. Therefore, it is considered that if the power level difference between the asynchronously colliding signals can be increased by beamforming using multiple antennas, the receiver performance using SIC can be improved.

5.4.1 Application of beam forming to asynchronous SIC

In the following section, the beamforming is performed with multiple antennas (ULA) on the satellite. Since the DOAs of the AIS signals are unknown at the receiver and they arrive asynchronously, it is possible to obtain good receive performance simply by applying the asynchronous SIC method for a single antenna to each beam output while changing the direction of the main beam. The M dimensional beamforming weighting vector for controlling the direction of main beam ϕ' is written as

$$\boldsymbol{w}(\phi') = \left[1, \mathrm{e}^{j\frac{2\pi d}{\lambda}\sin\phi'}, ..., \mathrm{e}^{j\frac{2\pi d}{\lambda}(M-1)\sin\phi'}\right]^{\mathrm{T}}, \tag{5.11}$$

and $\boldsymbol{W}_{\mathrm{BF}}$ denotes an $N \times M$ beamforming weighting matrix which consists of weighting vectors for N directions of the main beam $\phi_n(n = 0, 1, ..., N-1)$,

$$\boldsymbol{W}_{\mathrm{BF}} = \begin{bmatrix} \boldsymbol{w}^{\mathrm{T}}(\phi'_0) \\ \boldsymbol{w}^{\mathrm{T}}(\phi'_1) \\ \vdots \\ \boldsymbol{w}^{\mathrm{T}}(\phi'_{N-1}) \end{bmatrix}. \tag{5.12}$$

From the above, the equation holds for an N dimensional vector consisting of weighted output vector $\boldsymbol{y}_{\mathrm{BF}}(t) = \left[y_{\phi'_0}(t), y_{\phi'_1}(t), ..., y_{\phi'_{N-1}}(t) \right]^{\mathrm{T}}$:

$$\boldsymbol{y}_{\mathrm{BF}}(t) = \boldsymbol{W}_{\mathrm{BF}}\boldsymbol{r}(t). \tag{5.13}$$

Here, $\boldsymbol{r}(t) = [r_0(t), r_1(t), ..., r_{M-1}(t)]^{\mathrm{T}}$ is the M dimensional received signal vector at the multiple antennas of the satellite. Then, each element of weighted output vector $y_{\mathrm{BF}}(t)$ is input to the delay and frequency estimation process and the demodulation processes explained in the previous section are performed.

5.4.2   Result selection

The CRC results of the data demodulation are compared at "Result Selection". The demodulated bit sequences whose CRC results are OK are input to the amplitude, phase and BT product estimation processes and are used for generating the replicas. However, any identical bit sequence is excluded.

5.4.3   Phase estimation and cancellation for multiple antennas

In multi-antenna SIC, it is necessary to cancel the signals of each antenna, so it is necessary to estimate the phase differences between the antennas due to DOA. As a simple estimation method, the phase variation estimation described in Section 5.3 is applied to each antenna's signal.

$$\hat{\psi}_m(t) = \arg\left[\tilde{r}_m(t)z^*(t) \right]. \tag{5.14}$$

Here, $\hat{\psi}_m(t)$ may be estimated after applying a moving average filter to $\tilde{r}_m(t)z^*(t)$ in order to reduce any momentary variations. Using the above estimated value, canceling can be performed for each antenna's signal, and the received signal $\bar{r}_m(t)$ after canceling for each antenna can be obtained.

5.4.4   Further performance improvement for beamforming

Generally, in order to create a sharp main beam, the number of antenna elements may be increased. However, since the AIS signals are in the VHF band, it is not possible to use a large number of antennas due to the restricted antenna installation space on the satellite.

When AIS signals with little variation in DOA and the same signal strength are received, it is also difficult to separate them. Therefore, in order to separate closely aligned waves with a limited number of antenna elements, the proposed method introduces beam forming based on the Chebyshev distribution [85], [86].

Beam forming based on the Chebyshev distribution has the property of keeping the sidelobe level (SLL) constant and the SLL can be freely selected. Generally, when the SLL is high, the main beam width becomes narrow. Conversely, reducing the SLL broadens the main beam. Due to this property, when closely aligned waves are arriving, it is considered that the main beam should be sharpened by setting the SLL high based on the Chebyshev distribution beam forming. In addition, if there is some difference in signal strength between the closely aligned waves, they can be separated by the single antenna SIC, so it may be better to lower the sidelobe level to suppress interference from the surroundings. Therefore, more AIS signals can be separated by adding weights with different SLLs to the beamforming matrix. Here, new beamforming vectors and their matrix are defined as follows.

An M dimensional beamforming weighting vector whose SLL is L based on the Chebyshev distribution for controlling the direction of main beam ϕ' is written as

$$\boldsymbol{w}^{(L)}(\phi') = \left[s_0^{(L)}, s_1^{(L)} e^{j\frac{2\pi d}{\lambda}\sin\phi'}, ..., s_{M-1}^{(L)} e^{j\frac{2\pi d}{\lambda}(M-1)\sin\phi'} \right]^{\mathrm{T}}, \tag{5.15}$$

and $\boldsymbol{W}_{\mathrm{BF}}^{(L)}$ denotes the $N \times M$ Chebyshev distribution beamforming weighting matrix which consists of weighted vectors for N directions of the main beam $\phi'_n (n = 0, 1, ..., N-1)$,

$$\boldsymbol{W}_{\mathrm{BF}}^{(L)} = \begin{bmatrix} \boldsymbol{w}^{(L)\mathrm{T}}(\phi'_0) \\ \boldsymbol{w}^{(L)\mathrm{T}}(\phi'_1) \\ \vdots \\ \boldsymbol{w}^{(L)\mathrm{T}}(\phi'_{N-1}) \end{bmatrix}. \tag{5.16}$$

Here, the value of SLL L is relative to the peak of the main beam. Then, a new beamforming matrix $\boldsymbol{W}_{\mathrm{CBF}}$ is defined which consists of $\boldsymbol{W}_{\mathrm{BF}}$ and $\boldsymbol{W}_{\mathrm{BF}}^{(L)} (L = L_0, L_1..., L_{H-1})$:

$$\boldsymbol{W}_{\mathrm{CBF}} = \begin{bmatrix} \boldsymbol{W}_{\mathrm{BF}} \\ \boldsymbol{W}_{\mathrm{BF}}^{(L_0)} \\ \boldsymbol{W}_{\mathrm{BF}}^{(L_1)} \\ \vdots \\ \boldsymbol{W}_{\mathrm{BF}}^{(L_{H-1})} \end{bmatrix}. \tag{5.17}$$

$\boldsymbol{W}_{\mathrm{CBF}}$ is an $(H+1)N \times M$ beamforming weighted matrix with $H+1$ types of beamforming weights (H types SLL + uniform) for N desired directions ϕ'_n. In Figure 5.3, W_{CBF} is applied to the beamforming matrix module and the other processes operate in the same way.

Preamble (24bits)	Start flag (8bits)	Data (168bits)	CRC (16bits)	End flag (8bits)

Figure 5.4: AIS packet format. Reprinted from [13] with permission (©2022 IEEE).
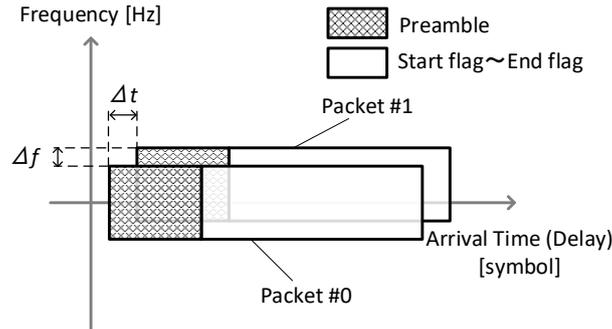

Figure 5.5: Time frequency relationship between two packets. Reprinted from [13] with permission (©2022 IEEE).

Table 5.1: Simulation parameters for single antenna case.

No. of RX antennas (M)	1
No. of interference packets (K)	2
P_0/P_N	10 - 20 dB
Time difference (Δt)	0 - 480 samples
Frequency difference (Δf)	0 - 8,000 Hz
Power difference (ΔP)	0 or 10 dB

5.5 Simulation

5.5.1 Simulation setup for single RX antenna

The packet error rate (PER) performance of the SIC for dealing with asynchronous signal collisions using a single RX antenna ($M = 1$) is evaluated by computer simulation. Table 5.1 shows the parameters used in the simulation. In this simulation, an environment in which two AIS signals collide asynchronously ($K = 2$) is assumed. The modulation of each signal is GMSK, and the BT product of the Gaussian filter used for GMSK modulation is 0.4. The receiver does not know the BT product of each AIS signal. The symbol rate is
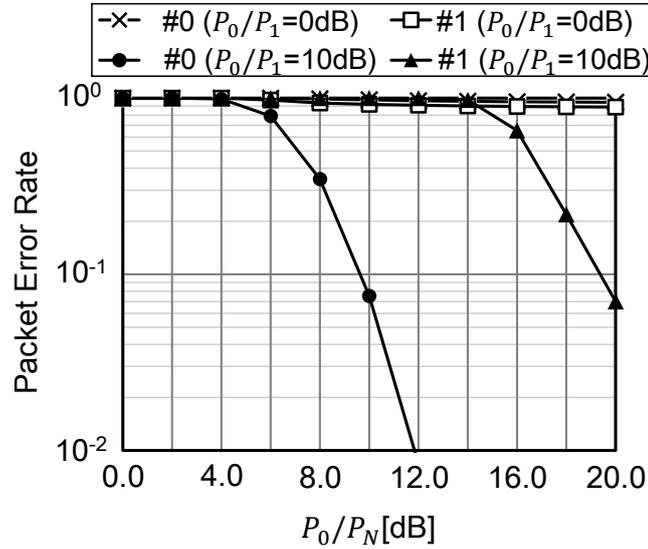
Figure 5.6: PER performance for single antenna. Reprinted from [13] with permission (ⓒ2022 IEEE).

Table 5.2: Simulation parameters for multiple antenna case.

No. of RX antennas (M)	6
No. of interference packets (K)	5, 7, 9
P_k/P_N	10 dB
Time difference (Δt)	0 sample
Frequency difference (Δf)	0 Hz
Power difference (ΔP)	0 dB
DOA difference ($\Delta \phi$)	10 degree
No. of main beam direction (N)	181 (1 degree interval)
No. of SLL (H)	2
Value of SLL (L)	-5, -20dB

9,600 and the number of oversamples (Q) is 8. In addition, it is an AWGN environment. Figure 5.4 shows the packet format of the AIS signals. The preamble is 24 bits long, both the start flag and end flag are 8 bits, 168 bits of data are randomly generated, and the CRC is 16 bits.

Figure 5.5 shows the relationship between the arrival time (delay) and frequency of the two colliding packets. Let the arrival time difference Δt of the two packets be a uniform
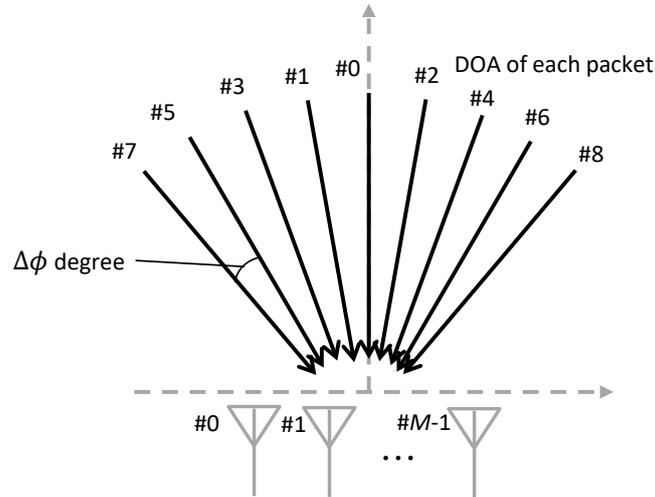
Figure 5.7: Relationship between DOA of each packet and the ULA of the satellite. Reprinted from [13] with permission (©2022 IEEE).

distribution from 0 to 60 symbols (0 to 480 samples) and let the arrival frequency difference Δf of the two packets be a uniform distribution from 0 to 8,000 Hz. The power difference (ΔP) between the two packets is fixed at 0 and 10 dB. Each AIS signal is affected by phase noise, and the standard deviation of the phase variation is 1 degree/symbol. The phase variation of the phase noise is modeled by the Wiener process [87]. The power of the kth packet is represented by P_k, and the power in the AWGN is represented by P_N. According to the AIS communication standard [78], the target PER at DUR (desired signal to undesired signal ratio) = 10 dB is 20%. In this evaluation, P_1/P_2 is set to eather 0 or 10 dB.

5.5.2 Simulation results for single RX antenna

Figure 5.6 shows the PER versus the signal to noise power ratio of Packet #0 (P_0/P_N) when the frequency difference Δf and the arrival time difference Δt are randomly changed. From this figure, it can be seen that when the power difference (ΔP) is 0 dB, it is almost impossible to demodulate the signals. This is because the interference power is too large to demodulate any wave, making it difficult to perform SIC. When the power difference (ΔP) is 10 dB, good performance is obtained for both Packet #0 and Packet #1. From the above, the proposed asynchronous SIC using a single RX antenna can separate colliding signals if there is a certain power difference ΔP.

5.5.3 Simulation setup for multiple RX antennas

Table 5.2 shows the parameters used in the simulation. The PER performance of the SIC for dealing with asynchronous signal collisions using multiple RX antennas ($M = 6$) is evaluated by computer simulation. In this simulation, it is assumed that 5, 7 and 9 AIS signals collide and are received as a number of arriving waves that exceeds the number of receiving antennas (when $K = 7, 9$). In addition, the power difference ΔP, and the time, and frequency difference Δt, Δf of each AIS signal are all set to 0. As can be seen from the simulation results in the previous section, the environment is considered to be heavily affected by interference. Figure 5.7 shows the relationship between DOA of each packet and the ULA of the satellite. When $K = 5$, the AIS packets from #0 to #4 arrive, when $K = 7$, the AIS packets from #0 to #6 arrive, and when $K = 9$, the packets from #0 to #8 arrive, all at $\Delta\phi = 10$ [degree] intervals. In this simulation, for the sake of simplicity, the assumptions that the phase fluctuation due to phase noise is 0 and that the BT product is unknown at the receiving side are excluded.

5.5.4 Simulation results for multiple RX antennas

Figures 5.8 and 5.11 show the relationship between P_k/P_N and the PER of each AIS packet when $K = 5$. Figure 5.8 shows the results when $\boldsymbol{W}_{\mathrm{BF}}$ is used for the beamforming matrix, and Figure 5.11 shows the results when $\boldsymbol{W}_{\mathrm{CBF}}$ is used for the beamforming matrix. In all the results, it can be seen that PER = 20% can be achieved under severe interference conditions ($\Delta t = 0, \Delta f = 0, \Delta P = 0$) that cannot be demodulated by SIC with a single antenna. In addition, it can be confirmed that better characteristics are obtained by using $\boldsymbol{W}_{\mathrm{CBF}}$.

Figures 5.9 and 5.12 show the relationship between P_k/P_N and the PER of each AIS packet when $K = 7$. In all the results, PER = 20% can be achieved. In addition, P_k/P_N which achieves a PER of 20% can be greatly improved by using $\boldsymbol{W}_{\mathrm{CBF}}$. It is considered that this is because the main beam width is changed by varying the SLL, and the power ratio between the packets becomes large, so the number of signals that can be demodulated increases. In addition, the PER performance of the packets located within deteriorates. This is because they are affected more by the interference because there are interfering waves on both sides.

Figures 5.10 and 5.13 show the relationship between P_k/P_N and the PER of each AIS packet when $K = 9$. When the number of arriving waves is large, the interference incident on the main beam with the same power level increases, so none of the packets can achieve PER = 20% when $\boldsymbol{W}_{\mathrm{BF}}$ is used. On the other hand, when $\boldsymbol{W}_{\mathrm{CBF}}$ is used, packets from #5 to #8 achieve PER = 20%, and the other packets' PERs are about 30-40%. It can be seen that the receiver performance can be improved even in an environment with more waves arriving.

Figure 5.14 shows the relationship between P_k/P_N and the PER of each AIS packet when $K = 9$ ($-20 \leq \Delta t \leq 20$ [symbol], $-20 \leq \Delta f \leq 20$ [%]). Here, Δt and Δf are generated with uniform distribution. In all the results, it can be confirmed that better

characteristics are obtained by using W_{CBF}. The improvement effect of the W_{CBF} is more pronounced when the time and frequency are randomized.

5.6 Conclusions

This paper describes the receiver performance of a new SIC for dealing with asynchronous collisions for a single antenna, and a method that increases the number of signal separations by combining this SIC with multi-antenna beamforming based on Chebyshev distribution. The simulation results show that our proposed method can improve the packet error rate even when the number of interference waves arriving is more than the number of receiving antennas.
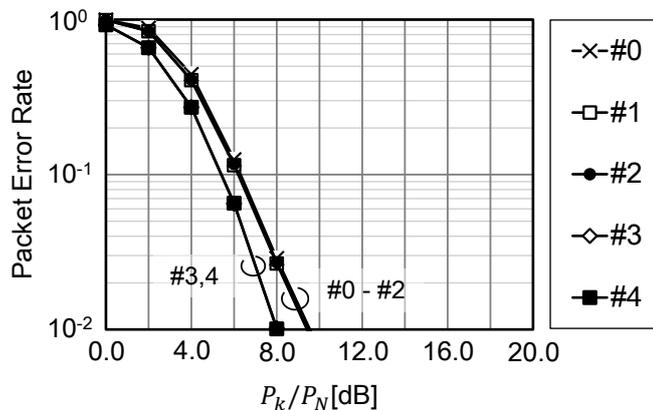
Figure 5.8: PER performance for multi-antenna ($K = 5, \boldsymbol{W}_{\mathrm{BF}}$). Reprinted from [13] with permission (©2022 IEEE).
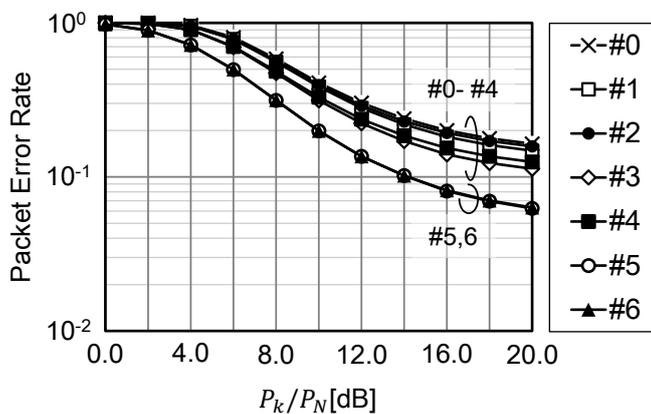
Figure 5.9: PER performance for multi-antenna ($K = 7, \boldsymbol{W}_{\mathrm{BF}}$). Reprinted from [13] with permission (©2022 IEEE).
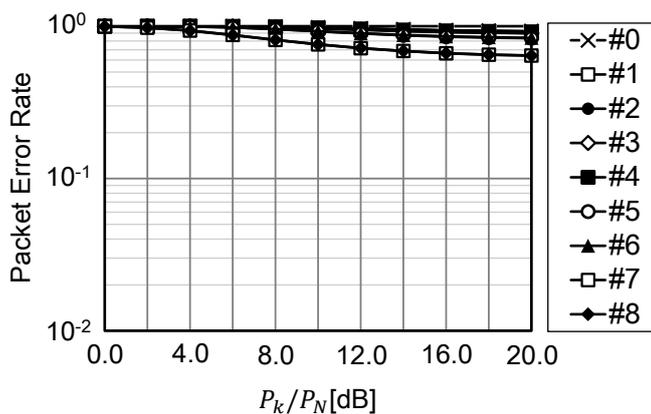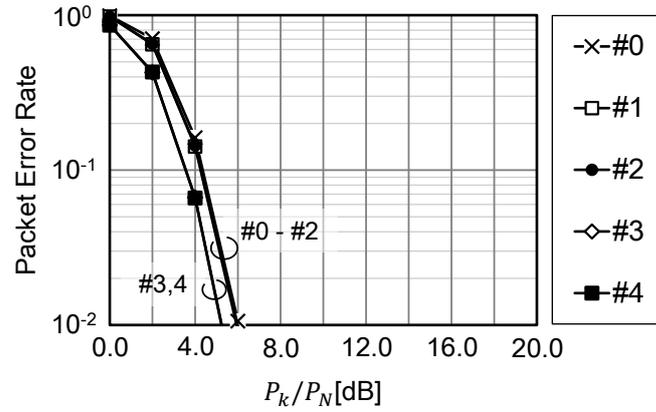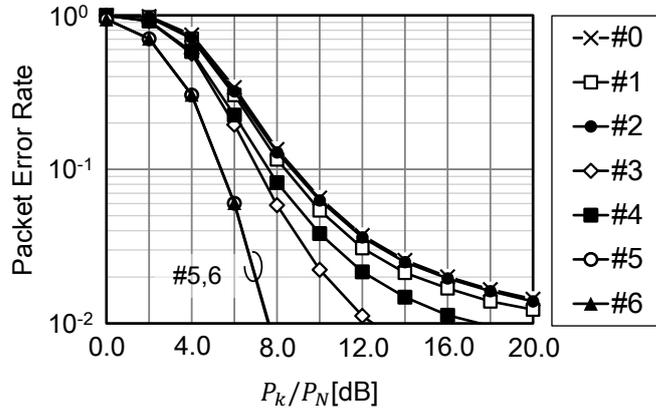

Figure 5.10: PER performance for multi-antenna ($K = 9, \boldsymbol{W}_{\mathrm{BF}}$). Reprinted from [13] with permission (©2022 IEEE).

Figure 5.11: PER performance for multi-antenna ($K = 5, \boldsymbol{W}_{\mathrm{CBF}}$). Reprinted from [13] with permission (ⓒ2022 IEEE).

Figure 5.12: PER performance for multi-antenna ($K = 7, \boldsymbol{W}_{\mathrm{CBF}}$). Reprinted from [13] with permission (ⓒ2022 IEEE).
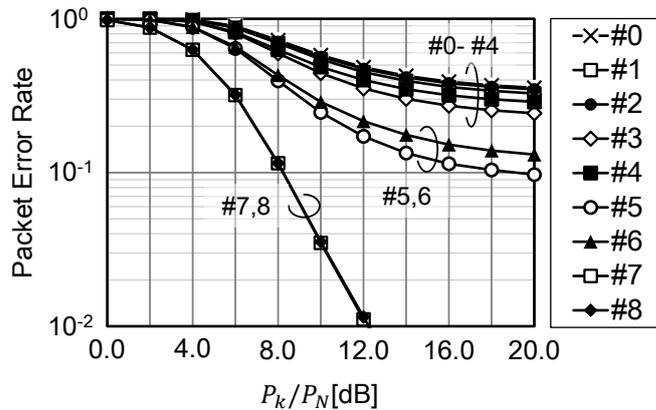

Figure 5.13: PER performance for multi-antenna ($K = 9, \boldsymbol{W}_{\mathrm{CBF}}$). Reprinted from [13] with permission (ⓒ2022 IEEE).
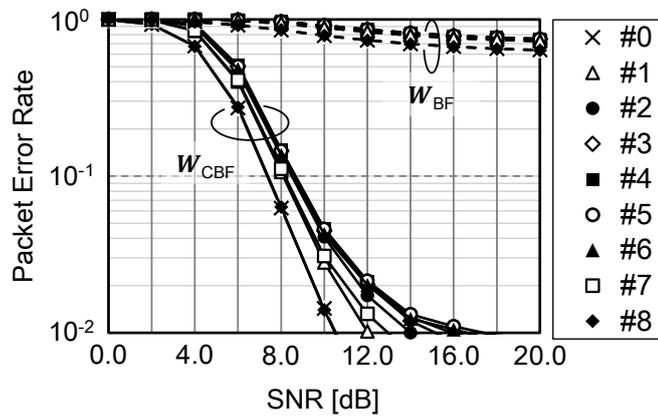
Figure 5.14: PER performance for multi-antenna ($K = 9$)..

Chapter 6

Conclusions

In this dissertation, the author has examined four methods to improve communication quality by converting the under-determined problem into some form of over-determined or determined problem in four different wireless communication systems.

First, Chapter 1 explained about the background and motivation of the dissertatio.

Chapter 2 proposes a novel channel prediction scheme in multi-user MIMO system. The under-determined problem is solved by increasing the virtual number of RX antennas and having a larger synthetic array using the observed signals obtained at multiple times. The proposed method is applied to a multi-user MIMO system, the method greatly improved the PER performance and throughput compared with the conventional methods.

In Chapter 3, this paper propose a CCI suppression method for DSTBC transmission. To overcome the under-determined problem in DSTBC, the proposed method increases the dimensionality of the RX signal vector by expanding the channel matrix and the RX signal vector based on the DSTBC coding rule. This converts the under-determined problem into the determined problem form to suppresses the interference. The results of our simulations show that the interference can be suppressed even when the number of arriving interference waves is more than twice the number of receiving antennas.

In Chapter 4, this paper proposes an adaptive nonlinear equalizer based on a memory polynomial. The evaluation results show improved receiver performance for 32APSK and 64APSK transmission in the presence of both nonlinear and linear distortion. The proposed method provides 1.3 dB (32APSK) and 1.7 dB (64APSK) improvement relative to a conventional linear equalizer. Moreover, this paper provides a method of reducing the number of nonlinear filter coefficients for further performance improvement and shows the effect of changing the roll-off factor in a satellite channel. These results verify the effectiveness of our proposed equalizer.

In Chapter 5, this paper describes the receiver performance of a new SIC for dealing with asynchronous collisions for a single antenna, and a method that increases the number of signal separations by combining this SIC with multi-antenna beamforming based

on Chebyshev distribution. The simulation results show that our proposed method can improve the packet error rate even when the number of interference waves arriving is more than the number of receiving antennas.

As described above, this paper presents approaches to solving the under-determined problems in four wireless communication systems by appropriately expanding the observed vector or reducing the unknown vector according to the system. With the recent proliferation of Internet of Things (IoT) systems, there will be more and more systems where the under-determined problem becomes an issue due to the huge number of devices. The solution of these problems based on the approach presented in this paper is expected to lead to further development of IoT systems and wireless communication systems.

References

[1] G. J. Foschini, "Layered Space-Time Architecture for Wireless Communication in a Fading Environment when using Multi-element Antennas," Bell Labs Tech. J., vol. 1, no. 2, pp. 41-59, Autumn 1996.

[2] G. J. Foschini and W. J. Gans, "On Limits of Wireless Communication in a Fading Environment when using Multiple Antennas," Wireless Personal Commun., vol. 6, no. 3, pp. 314-335, March 1998.

[3] M. Cetin, D. M. Malioutov, and A. S. Willsky, "A variational technique for source localization based on a sparse signal reconstruction perspective," *Proc. IEEE ICASSP*, vol. 3, pp. 2965–2968, May 2002.

[4] K. Hayashi, M. Nagahara, and T. Tanaka, "A user's guide to compressed sensing for communications systems," *IEICE Trans. Commun.*, vol. E96–B, no. 3, pp. 685–712, Mar. 2013.

[5] R. Hayakawa, K. Hayashi, "Asymptotic Performance of Discrete-Valued Vector Reconstruction via Box-Constrained Optimization With Sum of ℓ_1 Regularizers," IEEE Transactions on Signal Processing, vol.68, pp.4320-4335, 2020.

[6] K. Wong and A. Paulraj, "Efficient High-Performance Decoding for Overloaded MIMO Antenna Systems," IEEE Trans. on Wireless Commun., vol. 6, no. 5, pp. 1833-1843, May 2007.

[7] M. Hagiwara, T. Nishimura, T. Ohgane, and Y. Ogawa, "Node Selection for Belief Propagation Based Channel Equalization," IEICE Trans. Commun., vol. E100-B, no. 8, pp. 1285-1292, Aug. 2017.

[8] T. Takahashi, S. Ibi, and S. Sampei, "Design of Criterion for Adaptively Scaled Belief in Iterative Large MIMO Detection," IEICE Trans. Commun., vol. E102-B, no. 2, pp. 285-297, Feb. 2019.

[9] S. Uehashi, Y. Ogawa, T. Nishimura, and T. Ohgane, "Prediction of time-varying multi-user MIMO channels based on DOA estimation using compressed sensing," *IEEE Trans.Veh. Technol.*, vol. 68, no. 1, pp. 565—577, Jan. 2019.

[10] S. Uehashi, H. Nishimoto, K. Tomitsuka, H. Sano, and M. Hangai, "Co-channel inter-ference supression for DSTBC transmission in single frequency network," vol. J105-B, no. 5, pp. 446–453, May 2022.

[11] S. Uehashi, Y. Nouda, S. Tani, S. Uchida, and H. Aruga, "An adaptive equalization scheme based on memory polynomial for compensating both linear and nonlinear distortion," vol. J104-B, no. 3, pp. 271–279, March 2021.

[12] S. Uehashi, Y. Nouda, S. Tani, M. Hangai, and H. Aruga, "An adap-tive nonlinear equalizer utilizing memory polynomial for wideband satel-lite communications," IEEE Aerospace Conference 2021, March 2021, doi: 10.1109/AERO50100.2021.9438217

[13] S. Uehashi, Y. Nouda, M. Hangai, and T. Ohgane, "Successive Interference Can-cellation for Asynchronous Signal Collision in Space-based AIS," IEEE Aerospace Conference 2022, March 2022.

[14] S. Uehashi, Y. Ogawa, T. Nishimura, and T. Ohgane, "Channel prediction using 2-step compressed sensing in a time-varying multi-user MIMO environment," *IEICE Tech-nical Report*, vol. 115, no. 472, RCS2015–394, pp. 357–362, Mar. 2016 (in Japanese, without peer review).

[15] S. Uehashi, Y. Ogawa, T. Nishimura, and T. Ohgane, "Improvement of channel pre-diction using compressed sensing in a multi-user MIMO environment with moving scatterers," *Proc. 2016 IEICE General Conference*, B-5-119, p. 512, Mar. 2016 (in Japanese, without peer review).

[16] Q. H. Spencer, A. L. Swindlehurst, and M. Haadt, "Zero-forcing methods for down-link spatial multiplexing in multiuser MIMO channels," *IEEE Trans. Signal Process.,* vol. 52, no. 2, pp. 461–471, Feb. 2004.

[17] K. Miyashita, T. Nishimura, T. Ohgane, Y. Ogawa, Y. Takatori, and K. Cho, "High data-rata transmission with eigenbeam-space division multiplexing (E-SDM) in a MIMO channel," *Proc. IEEE VTC 2002 Fall*, vol. 3, pp. 1302–1306, Sept. 2002.

[18] F. Rusek, D. Persson, B. K. Lau, E. G. Larsson, T. L. Marzetta, O. Edfors, and F. Tufvesson, "Scaling up MIMO: Opportunities and challenges with very large arrays," *IEEE Signal Process. Mag.*, vol. 30, no. 1, pp. 40–60, Jan. 2013.

[19] A. Duel-Hallen, S. Hu, and H. Hallen, "Long-range prediction of fading signals: En-abling adaptive transmission for mobile radio channels," *IEEE Signal Process. Mag.*, vol. 17, no. 3, pp. 62–75, May 2000.

[20] S. Semmelrodt and R. Kattenbach, "Investigation of different fading forecast schemes for flat fading radio channels," *Proc. IEEE VTC 2003 Fall*, pp. 149–153, Oct. 2003.

[21] Z. Shen, J. G. Andrews, and B. L. Evans, "Short range wireless channel prediction using local information," *Proc. 37th Asilomar Conference on Signals, Systems and Computers*, pp. 1147–1151, Nov. 2003.

[22] M. Chen, T. Ekman, and M. Viberg, "New approaches for channel prediction based on sinusoidal modeling," *EURASIP J. Adv. Signal Process.*, vol. 2007, Article ID 49393, 2007.

[23] A. Duel-Hallen, "Fading channel prediction for mobile radio adaptive transmission systems," *Proc. IEEE*, vol. 95, no. 12, pp. 2299–2313, Dec. 2007.

[24] I. C. Wong and B. L. Evans, "Sinusoidal modeling and adaptive channel prediction in mobile OFDM systems," *IEEE Trans. Signal Process.,* vol. 56, no. 41, pp. 1601–1615, Apr. 2008.

[25] H. P. Bui, Y. Ogawa, T. Nishimura, and T. Ohgane, "Performance evaluation of a multi-user MIMO system with prediction of time-varying indoor channels," *IEEE Trans. Antennas and Propagat.* , vol. 61, no. 1, pp. 371–379, Jan. 2013.

[26] Q. Wang, L. J. Greenstein, L. J. Cimini, D. S. Chan, and A. Hedayat, "Multi-user and single-user throughputs for downlink MIMO channels with outdated channel state information," *IEEE Wireless Commun. Lett.,* vol. 3, no. 3, pp. 321–324, June 2014.

[27] K. Yamaguchi, H. P. Bui, Y. Ogawa, T. Nishimura, and T. Ohgane, "Channel prediction techniques for a multi-user MIMO system in time-varying environments," *IEICE Trans. Commun.*, vol. E97–B, no. 12, pp. 2747–2755, Dec. 2014.

[28] A. K. Papazafeiropoulos and T. Ratnarajah, "Deterministic equivalent performance analysis of time-varying massive MIMO systems," *IEEE Trans. Wireless Commun.*, vol. 14, no. 10, pp. 5795–5809, Oct. 2015.

[29] C. Kong, C. Zhong, A. K. Papazafeiropoulos, M. Matthaiou, and Z. Zhang, "Sum-rate and power scaling of massive MIMO systems with channel aging," *IEEE Trans., Commun.*, vol. 63, no. 12, pp. 4879–4893, Dec. 2015.

[30] R. O. Adeogun, P. D. Teal, and P. A. Dmochowski, "Extrapolation of MIMO mobile-to-mobile wireless channels using parametric-model-based prediction," *IEEE Trans. Veh. Technol.*, vol. 64, no. 10, pp. 4487–4498, Oct. 2015.

[31] L. Fan, Q. Wang, Y. Huang, and L. Yang, "Performance analysis of low-complexity channel prediction for uplink massive MIMO," *IET Commun.*, vol. 10, iss. 14, pp. 1744–1751, 2016.

[32] Z. Xu, M. Hofer, and T. Zemen, "A time-variant channel prediction and feedback framework for interference alignment," *IEEE Trans. Veh. Technol.*, vol. 66, no. 7, pp. 5961–5973, July 2017.

[33] T. S. Rappaport, S. Sun, R. Mayzus, H. Zhao, Y. Azar, K. Wang, G. N. Wong, J. K. Schulz, M. Samimi, and F. Gutierrez, "Millimeter wave mobile communications for 5G cellular：It will work!," *IEEE Access*, vol. 1, pp. 335–349, May 2013.

[34] S. Uehashi, Y. Ogawa, T. Nishimura, and T. Ohgane, "Considerations on channel prediction using compressed sensing," *Proc. 2014 IEICE Society Conference*, B-5-50, p. 321, Sept. 2014 (in Japanese, without peer review).

[35] S. Uehashi, Y. Ogawa, T. Nishimura, and T. Ohgane, "Considerations on channel prediction schemes using compressed sensing," *IEICE Technical Report*, vol. 114, no. 245, A·P2014–109, pp. 1–6, Oct. 2014 (in Japanese, without peer review).

[36] S. Uehashi, Y. Ogawa, T. Nishimura, and T. Ohgane, "Considerations on a channel prediction scheme using compressed sensing in multi-user MIMO systems," *IEICE Technical Report*, vol. 114, no. 395, RCS2014–278, pp. 55–60, Jan. 2015 (in Japanese, without peer review).

[37] S. Uehashi, Y. Ogawa, T. Nishimura, and T. Ohgane, "Channel prediction using compressed sensing in TDD multi-user MIMO systems," *Proc. 2015 IEICE General Conference*, B-5-19, p. 374, Mar. 2015 (in Japanese, without peer review).

[38] S. Uehashi, Y. Ogawa, T. Nishimura, and T. Ohgane, "Doppler frequency estimation and channel prediction using compressed sensing," *Proc. 2015 IEICE Society Conference*, B-5-10, p. 272, Sept. 2015 (in Japanese, without peer review).

[39] S. Uehashi, Y. Ogawa, T. Nishimura, and T. Ohgane, "Channel prediction using compressed sensing in a multi-user MIMO environment with moving scatterers," *IEICE Technical Report*, vol. 115, no. 288, RCS2015–240, pp. 299–304, Nov. 2015 (in Japanese, without peer review).

[40] S. Uehashi, Y. Ogawa, T. Nishimura, and T. Ohgane, "Channel prediction using compressed sensing in multi-user MIMO systems," *2016 International Conference on Computing, Networking and Communications (ICNC), Signal Processing for Communications (SPC)*, pp. 974–979, Feb. 2016.

[41] W. K. Ma, T. H. Hsieh, and C. Y. Chi, "DOA estimation of quasi-stationary signals with less sensors than sources and unknown spatial noise covariance: A Khatri-Rao subspace approach," *IEEE Trans. Signal Processing.*, vol. 58, no. 4, pp. 2168–2180, April 2010.

[42] J. Capon, "High resolution frequency-wavenumber spectrum analysis," *IEEE Proc.*, vol. 57, pp. 1408–1418, Mar. 1969.

[43] R. O. Schmidt, "Multiple emitter location and signal parameter estimation," *IEEE Trans. Antennas & Propagation*, vol. 34, no. 3, pp. 276–280, Mar. 1986.

[44] R. Roy and T. Kailath, "ESPRIT – Estimation of signal parameters via rotation invariance techniques," *IEEE Trans. Acoust., Speech, Signal Proc.*, vol. 17, no. 7, July 1989.

[45] B. H. Fleury, M. Tschudin, R. Heddergott, D. Dahlhaus, and K. I. Pedersen, "Channel parameter estimation in mobile radio environments using the SAGE algorithm," *IEEE J. Select. Areas Commun.*, vol. 17, no. 3, pp. 434–450, Mar. 1999.

[46] M. R. Akdeniz, Y. Liu, M. K. Samimi, S. Sun, S. Rangan, T. S. Rappaport, and E. Erkip, "Millimeter wave channel modeling and cellular capacity evaluation," *IEEE J. Select. Areas Commun.*, vol. 32, no. 6, pp. 1164–1179, June 2014.

[47] A. Forenza, D. J. Love, and R. W. Heath, Jr., "Simplified spatial correlation models for clustered MIMO channels with different array configurations," *IEEE Trans. Veh. Technol.*, vol. 56, no. 4, pp. 1924–1934, July 2007.

[48] S. Shirai, H. Yamada, and Y. Yamaguchi, "A novel DOA estimation error reduction preprocessing scheme of correlated waves for Khatri-Rao product extended-array," *IEICE Trans. Commun.*, vol. E96–B, no. 10, pp. 2475–2482, Oct. 2013.

[49] H. Yamada, M. Ohmiya, Y. Ogawa and K. Itoh, "Superresolution techniques for time-domain measurements with a network analyzer," *IEEE Trans. Antennas and Propagat.*, vol. 39, no. 2, pp. 177–183, Feb. 1991.

[50] J. Zhao, F. Gao, W. Jia, S. Zhang, S. Jin, and H. Lin, "Angle domain hybrid precoding and channel tracking for millimeter wave massive MIMO systems," *IEEE Trans. Wireless Commun.*, vol. 16, no. 10, pp. 6868–6880, Oct. 2017.

[51] H. Huang, J. Yang, H. Huang, Y. Song, and G. Gui, ."Deep learning for super-resolution channel estimation and DOA estimation based massive MIMO system," *IEEE Trans. Veh. Technol.*, vol. 67, no. 9, pp. 8549–8560, Sept. 2018

[52] L. Cheng, Y. C. Wu, J. Zhang, and L. Liu, "Subspace identification for DOA estimation in massive/full-dimension MIMO systems: Bad data mitigation and automatic source enumeration,," *IEEE Trans. Signal Process.*, vol. 63, no. 22, pp. 5897–5909, Nov. 2015.

[53] S. Alamouti, "A simple transmit diversity technique for wireless communications," IEEE J. Sel. Areas Commun.., vol.16, pp.1451–1458, Oct. 1998. DOI: 10.1109/49.730453

[54] V. Tarokh and H. Jafarkhani, "A differential detection scheme for transmit diversity," IEEE J. Sel. Areas in Commun., vol.18, no.7, pp.1169–1174, July 2000. DOI: 10.1109/49.857917

[55] B.L. Hughes, "Differential space-time modulation," IEEE Trans. Inf. Theory, vol.46, pp.2567—2578, Nov. 2000.
DOI: 10.1109/18.887864

[56] L. Chen, A. G. Helmy, G. Yue, S. Li and N. Al-Dhahir, "Performance analysis and compensation of joint TX/RX I/Q imbalance in differential STBC-OFDM," IEEE Trans. Veh. Technol., vol. 66, no. 7, pp. 6184–6200, July 2017.
DOI: 10.1109/TVT.2016.2639828

[57] S. K. Biswas, T. Taniguchi, and Y. Karasawa, "Macro-Diversity Scheme for a Point-to-Multipoint Communication System by means of D-STBC Method in Fast Fading Environment," IEICE Trans. Commun., vol.E92–B, no.6, pp.2122–2130, June 2009.
DOI: 10.1587/transcom.E92.B.2122

[58] S. Masuda, S. Sasaki, M. Higashinaka, and H. Aruga, "Beat Interference Suppression Method for Transmit Diversity," *Proc. 2020 IEICE General Conference*, B–5–16, March 2020.

[59] S. Sasaki, H. Sano, S. Masuda, and A. Okamura, "Phase Offset Method between Transmit Antennas for Avoiding Beat Interference in Differential Space-Time," *Proc. 2017 IEICE General Conference*, B–5–10, Sept. 2017.

[60] Y. Ohwatari, N. Miki, Y. Sagae, and Y. Okumura, "Investigation on interference rejection combining receiver for space-frequency block code transmit diversity in LTE-Advanced downlink," IEEE Trans. Veh. Technol., vol. 63, no. 1, pp. 191-203, Jan. 2014.
DOI: 10.1109/TVT.2013.2271508

[61] A. F. Naguib, N. Seshadri and A. R. Calderbank, "Applications of space–time block codes and interference suppression for high capacity and high data rate wireless systems," Conf. Rec. Asilomar Conf. Signals Syst. Comput., pp.1803–1810, Nov. 1998.
DOI: 10.1109/ACSSC.1998.751635

[62] Y. Ohwatari, N. Miki, T. Asai, T. Abe and H. Taoka, "Performance of advanced receiver employing interference rejection combining to suppress inter-cell interference in LTE-advanced downlink," Proc. IEEE Veh. Technol. Conf. (VTC Fall), pp. 1-7, Sep. 2011.
DOI: 10.1109/VETECF.2011.6093196

[63] R. Nakamura, Y. Nouda, S.Masuda, H. Sano and H. Ishizu, "Joint symbol timing and block timing synchronization scheme for transmit diversity," IEICE Trans. Commun., vol.J98-B, no.3, pp.294–306, March 2015.

[64] ETSI EN 302 307 V.1.2.1, Aug. 2009.

[65] ETSI TR 102 376-2 V.1.1.1, Nov. 2015.

[66] A. Gutierrez and W. E. Ryan, "Performance of adaptative volterra equalizers on nonlinear satellite channels," *IEEE International Conference on Communication*, vol. 1, pp. 488-492, June 1995.

[67] J. Malone and M. A. Wickert., "Practical Volterra equalizers for wideband satellite communications with TWTA nonlinearities," *IEEE Digital Signal Processing and Signal Processing Education Meeting (DSP/SPE)*, pp. 48-53, Jan. 2011.

[68] M. A. Jarajreh, E. Giacoumidis, I. Aldaya, S. T. Le, A. Tsokanos, Z. Ghassemlooy, N. J. Doran, "Artificial neural network nonlinear equalizer for coherent optical OFDM," *IEEE Photon. Technol. Lett.*, vol. 27, no. 4, pp. 387– 390, Feb. 2015.

[69] X. Feng, Y. Wang, T. Qi, and Y. Chen, "The Design of Satellite Equalizer Based on CNN," *IEEE 8th Joint International Information Technology and Artificial Intelligence Conference (ITAIC)*, pp.1647-1651, May 2019.

[70] S. Uehashi, Y. Nouda, S. Tani, S. Uchida, and H. Aruga, "Adaptive Nonlinear Equalization Based on a Memory Polynomial for Wideband Satellite Communication," *25th Ka and Broadband Communications Conference*，Oct. 2019．

[71] S. Uehashi, Y. Nouda, S. Tani, S. Uchida, and H. Aruga, "An Adaptive Equalization Scheme based on Memory Polynomial for Compensating both Linear and Nonlinear Distortion," *IEICE Trans. B*，March. 2021, doi: 10.14923/transcomj.2020GWP0004.

[72] L. Ding, G.T. Zhou, D.R. Morgan, Zhengxiang Ma, J.S. Kenney, Jaehyeong Kim, C.R. Giardinaet, "A robust digital baseband predistorter constructed using memory polynomials," *IEEE Trans. Commun.*, vol. 52, pp. 159-165, Jan. 2004.

[73] S. Haykin, "Adaptive Filter Theory," NJ: Prentice Hall, 1991.

[74] A. Bonnaud, E. Feltrin, and L. Barbiero, "DVB-S2 Extension: End-to-End Impact of Sharper Roll-Off Factor Over Satellite Link," *SPACOMM 2014*, pp. 36-41, Feb. 2014.

[75] M. Kojima, M. Nagasaka, Y. Suzuki, Yuki, Koizumi, K. Saito, S. Tanaka, "Experimental Verification of Prototype Equalizer for Non-linear Compensation over Satellite Channel," *TRANSACTIONS OF THE JAPAN SOCIETY FOR AERONAUTICAL AND SPACE SCIENCES, AEROSPACE TECHNOLOGY JAPAN*, vol. 16, pp. 248, 2018.

[76] Recommendation ITU–R M.1371-5.＂Technical characteristics for an automatic identification system using time division multiple access in the VHF maritime mobile frequency band,＂ITU, 2014.

[77] Recommendation ITU-R M.2084.＂Satellite detection of automatic identification system messages,＂ITU, 2007.

[78] Recommendation ITU-R M.2169.＂Improved satellite detection of AIS,＂ITU, 2009.

[79] P. Burzigotti, A. Ginesi, and G. Colavolpe, "Advanced Receiver Design for Satellite-Based AIS Signal Detection," *International Journal of Satellite Communications & Networking 30.2*, pp. 52–63, 2012.

[80] K. Nozaki, Y. Takanezawa, Y. Chang, K. Fukawa, and D. Hirahara, "Multiuser Detection of Collided AIS Packets with Accurate Estimates of Doppler Frequencies," *2021 IEEE 93rd Vehicular Technology Conference (VTC2021-Spring)*, 2021.

[81] M. Zhou, A. van der Veen, and R. van Leuken, "Multi-user LEO-satellite receiver for robust space detection of AIS messages," *in Proc. IEEE Int. Conf. Acoust., Speech, and Signal Processing*, vol. 37, pp. 2529-2532, March 2012.

[82] M. Picard, M. R. Oularbi, G. Flandin, and S. Houcke, "An adaptive multi-user multi-antenna receiver for satellite-based AIS detection," *ASMS/SPSC 2012*, pp. 273-280, 2012.

[83] R. Prévost, M. Coulon, D. Bonacci, J. LeMaitre, J.-P. Millerioux and J.-Y. Tourneret, "Joint phase-recovery and demodulation-decoding of ais signals received by satellite," *Proc. on IEEE Int. Conf. ICASSP*, pp. 4913-4917, May 2013.

[84] E. Ip and J. Kahn, "Feedforward carrier recovery for coherent optical communications", *J. Lightw. Technol.*, vol. 25, Sept. 2007,

[85] C. L. Dolph, "A Current Distribution for Broadside Arrays Which Optimizes the Relationship Between Beamwidth and Side-Lobe Level," *Proc. IRE and Electrons*, June 1946.

[86] C. A. Balanis, "Antenna Theory", John Wiley & Sons, Inc., 2nd ed., 1982.

[87] A. Hassanin, F. Lazaro, and S. Plass, "An Advanced AIS Receiver using a Priori Information," OCEANS 2015, pp. 1–7, May 2015.

Acknowledgement

Shunsuke Uehashi

September 2022

List of Publications and Awards

Journals

[1] S. Uehashi, Y. Ogawa, T. Nishimura, and T. Ohgane, "Prediction of Time-varying Multi-user MIMO Channels Based on DOA Estimation Using Compressed Sensing," IEEE Trans. Veh. Technol, vol. 68, no. 1, pp. 565–577, Jan. 2019. doi: 10.1109/TVT.2018.2882214

[2] S. Uehashi, Y. Nouda, S. Tani, S. Uchida, and H. Aruga, "An Adaptive Equalization Scheme Based on Memory Polynomial for Compensating Both Linear and Nonlinear Distortion," IEICE Trans. Commun. (Japanese Edition), vol.J104-B, no.3, pp.271–279, Mar. 2021. doi: 10.14923/transcomj.2020GWP0004

[3] S. Uehashi, H. Nishimoto, K. Tomitsuka, Y. Sano, and M. Hangai, "Co-Channel Interference Suppression for DSTBC Transmission in Single Frequency Network," IEICE Trans. Commun. (Japanese Edition), vol.J105-B, no.5, pp.446–453, May 2022. doi: 10.14923/transcomj.2021JBP3020

International Conference

[1] S. Uehashi, Y. Ogawa, T. Nishimura, and T. Ohgane, "Channel Prediction Using Compressed Sensing in Multi-User MIMO Systems," Proc. ICNC 2016 SPC, pp. 974–979, Feb. 2016.

[2] S. Uehashi, Y. Nouda, S. Tani, S. Uchida, and H. Aruga, "Adaptive Nonlinear Equalization Based on a Memory Polynomial for Wideband Satellite Communication," Proc. 25th Ka and Broadband Communications Conference, Oct. 2019.

[3] S. Uehashi, Y. Nouda, S. Tani, M. Hangai, and H. Aruga, "An Adaptive Nonlinear Equalizer Utilizing Memory Polynomial for Wideband Satellite Communications," Proc. IEEE Aerospace Conference 2021, Mar. 2021.

[4] S. Uehashi, Y. Nouda, M. Hangai, and T. Ohgane, "Successive Interference Cancellation for Asynchronous Signal Collision in Space-based AIS," Proc. IEEE Aerospace Conference 2022, Mar. 2022.

Domestic Conference

[1] S. Uehashi, Y. Ogawa, T. Nishimura, and T. Ohgane, "Considerations on Channel Prediction Using Compressed Sensing," Proceedings of the 2014 IEICE Society Conference, B-5-50, Sept. 2014 (in Japanese).

and 17 others.

Awards

[1] 2015 IEICE RCS Active Research Award, 2016.

[2] 2021 Young Researchers' Award, IEICE, 2022.